An Improved Phase-Shifted Carrier Modulation Scheme for a Hybrid Modular Multilevel Converter

Sizhao Lu, *Student Member, IEEE*, Liqiang Yuan, *Member, IEEE*, Kai Li, *Student Member, IEEE*, and Zhengming Zhao, *Senior Member, IEEE*

***Abstract*—This paper presents an improved phase-shifted carrier pulse width modulation (PSC-PWM) scheme for the hybrid modular multilevel converter (MMC) consisting of half-bridge submodules (HBSMs) and full-bridge submodules (FBSMs). When the traditional PSC-PWM schemes for the HBSMs-based MMC and the FBSMs-based MMC are directly applied to the hybrid MMC, some mismatch pulses will occur on the arm voltages because the HBSMs and the FBSMs have different characteristics. These mismatch pulses not only generate undesirable harmonics on the output voltages, but also induce the significantly uneven loss distributions between the HBSMs and the FBSMs. Therefore, an improved PSC-PWM scheme for the hybrid MMC is proposed in this paper to deal with these issues. The improved PSC-PWM scheme can eliminate the mismatch pluses in the output voltages, alleviate the uneven loss distributions between the HBSMs and the FBSMs, and reduce the total switching loss of the converter. The mathematical analysis of the improved PSC-PWM scheme for the hybrid MMC is conducted and its harmonic characters are investigated. The analysis results are verified and compared with the traditional PSC-PWM scheme by the simulated and experimental results.**

***Index Terms*—Hybrid MMC, mismatch, phase-shifted carrier, pulse width modulation.**

I. Introduction

THE modular multilevel converter (MMC), first proposed in [1], is the most attractive topology for high-power high-voltage applications [2]–[4] because of its modular structure, high efficiency, and low harmonic distortion of the output waveforms. The basic operation principles of the MMC are given in [5] and [6]. Many basic circuit topologies can be employed as submodules (SMs) of the MMC. The most popular one is the half-bridge submodule (HBSM) because of its simple, low component number, and high efficiency. However, the HBSMs-based MMC is unable to limit the fault current during the dc-side short-circuit condition [7], [8]. The implementation of the HBSMs-based MMC is limited in the applications where dc-side short-circuit protection is required. Therefore, various modified SMs, such as the full-bridge submodule (FBSM) [9], the clamp-double SMs [10], the diode clamp SMs [11], unipolar voltage FBSMs [12], five-level cross-connected HBSMs [13], and three-level cross-connected SMs [12] are proposed to realize the dc-side short-circuit protection. However, these modified SMs employ more power devices compared with the HBSMs-based MMC and suffer from the high conduction loss [14]. To reduce the number of power devices and the conduction loss, the modified SMs and the HBSMs are mixed to form the hybrid MMCs. In [12], the unipolar-voltage FBSMs or the three-level cross-connected SMs are mixed with HBSMs to reduce the power devices number and the extra power losses. These two hybrid MMC topologies can control the dc fault current to be null but lose the ability to control the ac current during the dc-side fault condition. Therefore, they have the dc-side fault blocking capability but do not have the dc-side fault ride-through capability [15]. The hybrid MMC composed of the HBSMs and the FBSMs not only can control the dc fault current to be zero but also can control the ac grid-side reactive power to support the ac grid during the dc-side fault condition, that is, the dc-side fault ride-through capability [15], [16]. So it is a very promising topology for the next generation of highly meshed multiterminal HVdc grids [17].

Two major tasks associated with the MMC are the capacitor voltage balance and the circulating current suppression [18], and many papers have been published to tackle these two tasks for the HBSMs-based MMC [19]–[26], the FBSMs-based MMC [27], and the hybrid MMC [15], [17], [28], [29]. In addition, the pulse width modulation (PWM) scheme is one of the most interesting topics in the MMC [30]. Many PWM schemes have been proposed for the MMC. Space-vector modulation is first mentioned to be a possible modulation scheme for the MMC [6], but the calculation and selection of the vectors become very complicated as the SMs increase. The nearest level modulation (NLM) is especially suitable for the applications with a large number of SMs [22], [31]–[33]. In NLM, a round function is applied to find the required output voltage level, which introduces the round errors. To compensate the round errors, NLM is extended by introducing one SM working in the PWM mode [34]. The level-shifted PWM, known as phase-disposition PWM (PD-PWM), is also investigated in [35] and [36]. The main drawback of the level-shifted modulation is the uneven loss distribution among the SMs [37], [38], which is not desirable for the MMC. The phase-shifted carrier PWM (PSC-PWM) is another popular PWM scheme. Although it has been reported that the output voltage harmonic profile of the PD-PWM is better than that of the PS-PWM [39], these differences in the high-frequency harmonic contents are very small [37]. Therefore, PS-PWM is a very popular modulation scheme in the MMC because it offers some distinctive features [38], [40], [41].

Manuscript received June 9, 2015; revised November 10, 2015 and December 24, 2015; accepted February 7, 2016. Date of publication February 19, 2016; date of current version September 16, 2016. This work was supported in part by the Major Program of the National Natural Science Foundation of China (51490683) and in part by the Program of State Key Laboratory of Power System in Tsinghua University (SKLD15Z01). Recommended for publication by Associate Editor M. Saeedifard.

The authors are with the State Key Laboratory of Power System, Department of Electrical Engineering, Tsinghua University, Beijing 100084, China (e-mail: lusizhao6103@126.com; ylq@tsinghua.edu.cn; kevinlee1988@126.com; zhaozm@tsinghua.edu.cn).

Color versions of one or more of the figures in this paper are available online at http://ieeexplore.ieee.org.

Digital Object Identifier 10.1109/TPEL.2016.2532386

1) The power handled by each SM is the same as that of the other SMs, so the power loss is distributed evenly among the SMs.
2) The actual switching frequency of each power device equals the carrier frequency. The effective switching frequency is equal to the product of the number of cells and the carrier frequency of each cell, which results in a high effective switching frequency and low total harmonic distortion.
3) Consistent with the modularity and scalability of the MMC, it is easy to increase the number of SMs per arm.

The PSC-PWM is proved as an effective PWM solution for the HBSMs-based MMC and the FBSMs-based MMC. However, most of the existing literatures about the PSC-PWM schemes only focus on the HBSMs-based MMC or the FBSMs-based MMC. To the knowledge of the authors, the PSC-PWM schemes for the hybrid MMC have not been studied in details in the previous literatures. In the hybrid MMC, each arm consists of HBSMs and FBSMs, which have different characteristics. When the PSC-PWM schemes used in the HBSMs-based MMC and the FBSMs-based MMC are directly applied to the hybrid MMC, two issues should be overcome. The first issue is that the number of the power devices in the FBSM is twice the number in the HBSM. When the same carrier frequency is employed for the HBSM and the FBSM, the output equivalent switching frequency of the FBSM is double that of the HBSM. Therefore, the total switching loss of the FBSM is also double that of the HBSM, which induces significantly uneven loss distribution between the HBSMs and the FBSMs. The second issue is that some mismatch pulses will occur on the arm voltages due to the different equivalent switching frequencies of the FBSM and the HBSM. These mismatch pulses are undesirable because they lower the center frequency of the lowest harmonic group in the output voltage, which reduces the cutoff frequency of the filter. The size of the filter is inevitably enlarged in order to attenuate these harmonics. In this paper, the traditional PSC-PWM scheme is first applied to the hybrid MMC and its characteristics are analyzed. Then, an improved PSC-PWM scheme for the hybrid MMC is proposed to deal with the issues associated with the traditional PSC-PWM scheme implemented in the hybrid MMC. The aim of this paper is to provide the detailed analysis of the PSC-PWM scheme in the hybrid MMC and to extend the well-proved PSC-PWM scheme to the hybrid MMC.

The remainder of this paper is organized as follows. The basic operating principles of the hybrid MMC is given in Section II. The traditional PSC-PWM scheme for the hybrid MMC is applied and analyzed in Section III-A. The improved PSC-PWM scheme is presented and its harmonic characters are analyzed in Section III-B. Simulated results are presented in Section IV. The experimental results on a hybrid MMC prototype are given in Section V. The conclusions are drawn in Section VI.

II. Basic Operating Principles of Hybrid MMC

A. Structure of a Hybrid MMC

The diagram of the hybrid MMC is depicted in Fig. 1. The MMC is formed by six arms. Each arm contains N SMs, which combines H HBSMs and F FBSMs ($N = H+F$). These SMs are connected in series and interfaced with the dc link by the arm inductors. The coupled inductor is used as the arm inductor, in this paper, due to its smaller size and weight compared with the discrete inductors [42]. The dc capacitors in the SMs act as the constant dc voltage sources, and the output voltages are synthesized by these constant dc voltage sources under the proper control.

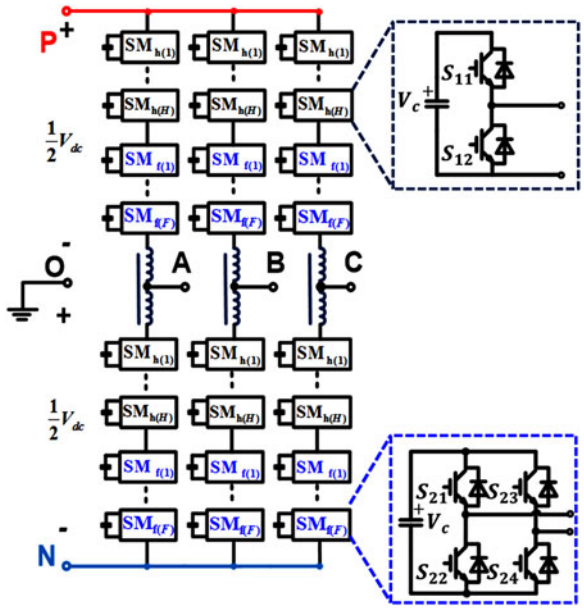

Fig. 1. Structure of a hybrid MMC.

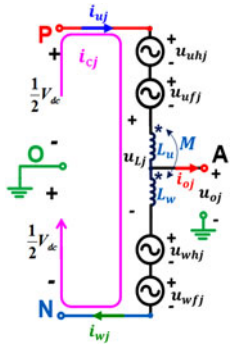

Fig. 2. Equivalent circuit of one phase of hybrid MMC.

B. Mathematic Model of Hybrid MMC

The equivalent circuit of one phase of the hybrid MMC is shown in Fig. 2. $V_{\rm dc}$ is the dc-link voltage, $i_{\rm oj}$ $(j = a, b, c)$ is the output current of phase j, and $u_{\rm oj}$ is the output phase voltage. $u_{\rm uhj}$, $u_{\rm ufj}$ and $u_{\rm whj}$, $u_{\rm wfj}$ represent the voltages generated by the HBSMs and FBSMs in the upper arm and the lower arm. $i_{\rm uj}$ and $i_{\rm wj}$ represent the currents of the upper arm and the lower arm, respectively. M and L_u, L_w are the mutual inductance and self-inductances. $u_{\rm Lj}$ is the voltage across the coupled inductor.

Assuming the coupled inductor is fully coupled (i.e., $L_u = L_w = M = L_o$), the following equations can be derived [40]:

$$u_{\mathrm{oj}} = \frac{1}{2}\left(u_{\mathrm{whj}} + u_{\mathrm{wfj}}\right) - \frac{1}{2}\left(u_{\mathrm{uhj}} + u_{\mathrm{ufj}}\right) = \frac{1}{2}\left(u_{\mathrm{wj}} - u_{\mathrm{uj}}\right) \quad (1)$$

$$u_{\mathrm{Lj}} = -u_{\mathrm{wj}} - u_{\mathrm{uj}} + V_{\mathrm{dc}} = 4L_o\frac{di_{\mathrm{cj}}}{dt} \quad (2)$$

where u_{wj}, u_{uj} are the lower arm voltage and the upper arm voltage, and i_{cj} is the circulating current of phase *j*. The circulating current flows through both the upper arm and the lower arm and it can be expressed as

$$i_{\mathrm{cj}} = \frac{1}{2}\left(i_{\mathrm{uj}} + i_{\mathrm{wj}}\right). \quad (3)$$

According to (2), the following equation can be derived:

$$i_{\mathrm{cj}} = I_{\mathrm{cj}} + \int_0^t \frac{u_{\mathrm{Lj}}}{4L_o}dt \quad (4)$$

where I_{cj} is the dc component of the circulating current. The output current is shared equally by the upper arm current and the lower arm current, so the upper arm current and the lower arm current are expressed as

$$i_{\mathrm{uj}} = i_{\mathrm{cj}} + \frac{1}{2}i_{\mathrm{oj}} \quad (5)$$

$$i_{\mathrm{wj}} = i_{\mathrm{cj}} - \frac{1}{2}i_{\mathrm{oj}}. \quad (6)$$

Based on the mathematical model of the hybrid MMC, the harmonic features of the converter can be investigated under a specific PSC-PWM scheme.

III. PSC-PWM Schemes for Hybrid MMC

A. Traditional PSC-PWM Scheme for Hybrid MMC

The detailed analysis of the traditional PSC-PWM scheme for the HBSMs-based MMC and the FBSMs-based MMC is given in [40]. Since the hybrid MMC combines both the HBSMs and FBSMs, the traditional PSC-PWM schemes for the HBSMs and the FBSMs is directly applied to the hybrid MMC, which is called the traditional modulation scheme for the hybrid MMC in this paper. However, some issues are encountered when the traditional PSC-PWM schemes for the HBSMs and the FBSMs are directly used in the hybrid MMC. Take the combination of single HBSM and single FBSM in the hybrid arm, as an example, which is shown in Fig. 3.

The voltage $u_{r\_\mathrm{uj}}(i)$ represents the reference signal of the HBSM, and $u_{r\_\mathrm{uj\_left}}(i)$ and $u_{r\_\mathrm{uj\_right}}(i)$ represent the reference signals of the left leg and the right leg of the FBSM. Note two reference signals are employed for the FBSM in Fig. 3 in order to generate two voltage levels 0 and V_{dc}/N, the same as that of the HBSM, and to achieve more even loss distribution among the devices. Because the output equivalent switching frequency of the HBSM is different from that of the FBSM when the same switching frequency is employed for both the HBSM and the FBSM, some mismatch pulses will occur on the output voltages, which are highlighted by the circles in Fig. 3(b). Moreover, these mismatch pulses cannot be eliminated by adjusting the phase-shifting angle between the HBSM and the FBSM. Although some mismatch pulses are generated in the arm voltages, the circulating current switching harmonics and the output voltage harmonics are determined by both the upper arm voltage and the lower arm voltage. So the circulating current harmonics cancellation and the output voltage harmonics minimization can be achieved by adjusting the displacement angle between the upper arm and the lower arm.

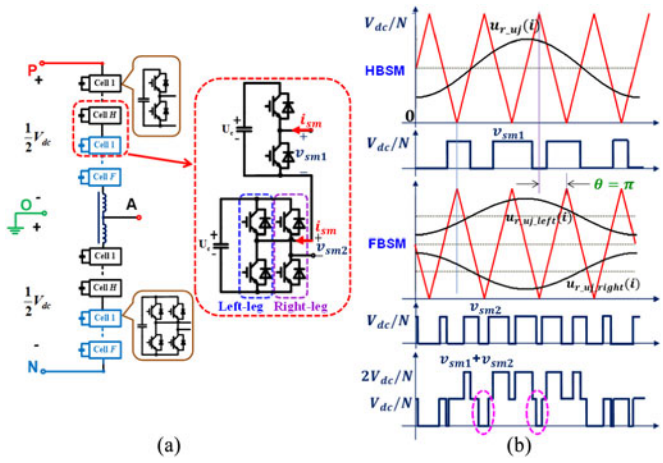

Fig. 3. Output voltage of hybrid arm composed of single HBSM and single FBSM with traditional PSC-PWM scheme.

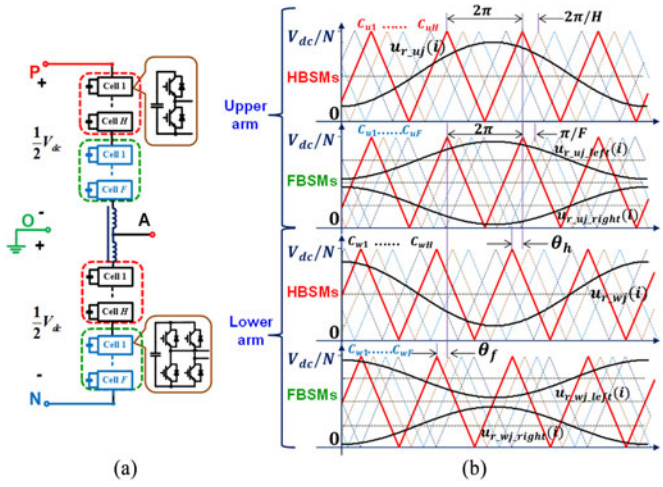

Fig. 4. Traditional PSC-PWM modulation scheme for a hybrid MMC.

The traditional PSC-PWM scheme for the hybrid MMC is shown in Fig. 4. To achieve the best harmonic cancellation effect, the triangular carriers of *H* HBSMs and *F* FBSMs in each arm are shifted by $2\pi/H$ and π/F, respectively. Because the mismatch pulses in the arm voltages cannot be eliminated by adjusting the phase-shifting angle between the HBSM and the FBSM in the arm, the phase-shifting angle between the

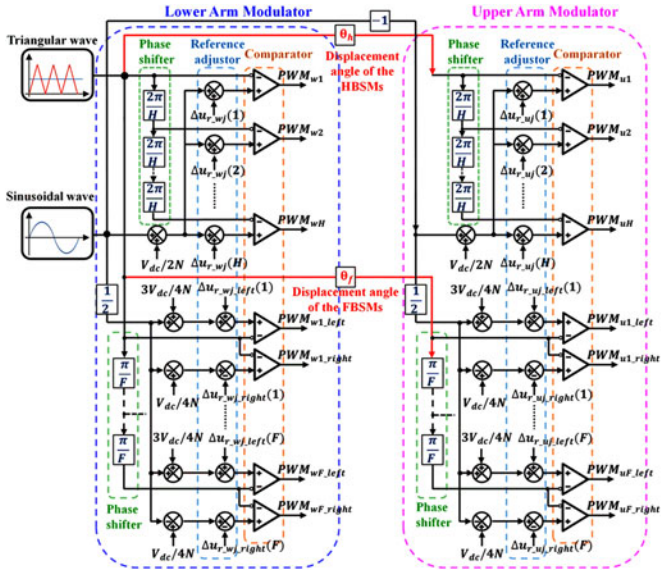

Fig. 5. Modulation signal distribution of traditional PSC-PWM for a hybrid MMC.

HBSMs and the FBSMs in the lower arm is simply selected as zero in this modulation scheme. The displacement angles of the HBSMs and the FBSMs between the upper arm and the lower arm are θ_h and θ_f, respectively. Accordingly, the modulation signal distribution of the traditional PSC-PWM for the hybrid MMC is shown in Fig. 5. The reference signals of the *i*th HBSM in the lower arm and the *i*th HBSM in the upper arm are given by

$$u_{\mathrm{ref\_wj}}(i) = \frac{V_{\mathrm{dc}}}{2N}(1 + M\cos(\omega_o t + \varphi_j)) + \Delta u_{r\_h\_\mathrm{wj}}(i) \tag{7}$$

$$u_{\mathrm{ref\_uj}}(i) = \frac{V_{\mathrm{dc}}}{2N}(1 + M\cos(\omega_o t + \varphi_j + \pi)) + \Delta u_{r\_h\_\mathrm{uj}}(i) \tag{8}$$

where M $(0 \le M \le 1)$ is the modulation index, ω_0 is the angular frequency of the output ac voltage, and φ_j is the phase angle.$\Delta u_{r\_h\_\mathrm{wj}}(i)$ and $\Delta u_{r\_h\_\mathrm{uj}}(i)$ represent the adjustments of the reference signal for each HBSM in the lower arm and the upper arm.

These adjustments of the reference signals are used to balance the voltages of the HBSMs and they can be expressed as

$$\Delta u_{r\_h\_\mathrm{wj}}(i) = \begin{cases} K_p\left(U_C - U_{c\_h\_\mathrm{wj}}(i)\right), & i_{\mathrm{wj}} > 0 \\ -K_p\left(U_C - U_{c\_h\_\mathrm{wj}}(i)\right), & i_{\mathrm{wj}} < 0 \end{cases} \tag{9}$$

$$\Delta u_{r\_h\_\mathrm{uj}}(i) = \begin{cases} K_p\left(U_C - U_{c\_h\_\mathrm{uj}}(i)\right), & i_{\mathrm{uj}} > 0 \\ -K_p\left(U_C - U_{c\_h\_\mathrm{uj}}(i)\right), & i_{\mathrm{uj}} < 0 \end{cases} \tag{10}$$

where K_p is the proportional gain, U_c is the capacitor voltage command, $U_{c\_h\_\mathrm{wj}}(i)$ is the capacitor voltage of *i*th HBSM in the lower arm, i_{wj} is the arm current of the lower arm, $U_{c\_h\_\mathrm{uj}}(i)$ is the capacitor voltage of *i*th HBSM in the upper arm, and i_{uj} is the arm current of the lower arm. Equations (9) and (10) indicate that for the HBSM with the voltage lower than the command voltage, when the arm current is positive, the product of the adjustment voltage and the arm current will form a positive active power to charge the capacitor. When the arm current is negative, the polarity of the adjustment voltage should be accordingly changed in order to get the positive active power to charge the capacitor. In contrast, a negative active power should be generated to discharge the HBSM with the voltage higher than the command voltage.

The reference signals of the *i*th FBSM in the lower arm and the *i*th FBSM in the upper arm are given by (11) and (12), shown at the bottom of the page, where $\Delta u_{r\_f\_\mathrm{wj}}(i)$ and $\Delta u_{r\_f\_\mathrm{uj}}(i)$ represent the adjustment of the reference signal for each FBSM in the lower arm and the upper arm. These adjustments of the reference signals are used to balance the voltages of the FBSMs and they can be expressed as

$$\Delta u_{r\_f\_\mathrm{wj}}(i) = \begin{cases} K_p\left(U_C - U_{c\_f\_\mathrm{wj}}(i)\right), & i_{\mathrm{wj}} > 0 \\ -K_p\left(U_C - U_{c\_f\_\mathrm{wj}}(i)\right), & i_{\mathrm{wj}} < 0 \end{cases} \tag{13}$$

$$\Delta u_{r\_f\_\mathrm{uj}}(i) = \begin{cases} K_p\left(U_C - U_{c\_f\_\mathrm{uj}}(i)\right), & i_{\mathrm{uj}} > 0 \\ -K_p\left(U_C - U_{c\_f\_\mathrm{uj}}(i)\right), & i_{\mathrm{uj}} < 0 \end{cases} \tag{14}$$

where K_p is the proportional gain, U_c is the capacitor voltage command, $U_{c\_f\_\mathrm{wj}}(i)$ is the capacitor voltage of *i*th FBSM in the lower arm, i_{wj} is the arm current of the lower arm, $U_{c\_f\_\mathrm{uj}}(i)$ is the capacitor voltage of *i*th FBSM in the upper arm, and i_{uj} is the arm current of the lower arm. Equations (13) and (14) indicate the same voltage balance principle as (9) and (10).

$$\begin{cases} u_{\mathrm{ref\_wj\_left}}(i) = \dfrac{3V_{\mathrm{dc}}}{4N} + \dfrac{V_{\mathrm{dc}}}{4N}M\cos(\omega_o t + \varphi_j) + \Delta u_{r\_f\_\mathrm{wj}}(i) \\ u_{\mathrm{ref\_wj\_right}}(i) = \dfrac{V_{\mathrm{dc}}}{4N} + \dfrac{V_{\mathrm{dc}}}{4N}M\cos(\omega_o t + \varphi_j + \pi) - \Delta u_{r\_f\_\mathrm{wj}}(i) \end{cases} \tag{11}$$

$$\begin{cases} u_{\mathrm{ref\_uj\_left}}(i) = \dfrac{3V_{\mathrm{dc}}}{4N} + \dfrac{V_{\mathrm{dc}}}{4N}M\cos(\omega_o t + \varphi_j + \pi) + \Delta u_{r\_f\_\mathrm{uj}}(i) \\ u_{\mathrm{ref\_uj\_right}}(i) = \dfrac{V_{\mathrm{dc}}}{4N} + \dfrac{V_{\mathrm{dc}}}{4N}M\cos(\omega_o t + \varphi_j) - \Delta u_{r\_f\_\mathrm{uj}}(i) \end{cases} \tag{12}$$

In the following analysis, the capacitor voltages of all the SMs are assumed to be well balanced (i.e., $\Delta u_{r\_h\_\mathrm{wj}}(i) = \Delta u_{r\_h\_\mathrm{uj}}(i)=0$ and $\Delta u_{r\_f\_\mathrm{wj}}(i)=\Delta u_{r\_f\_\mathrm{uj}}(i)=0$). Therefore, the dc-link voltage V_{dc} will be evenly shared by the SMs (i.e., $U_{\mathrm{c}} = V_{\mathrm{dc}}/N$). Generally, $\Delta u_{r\_h\_\mathrm{wj}}(i)$, $\Delta u_{r\_h\_\mathrm{uj}}(i)$, and $\Delta u_{r\_f\_\mathrm{wj}}(i)$, $\Delta u_{r\_f\_\mathrm{uj}}(i)$ are a relatively small portion compared with the reference voltage signals (i.e., $u_{\mathrm{ref\_wj}}(i)$, $u_{\mathrm{ref\_uj}}(i)$, $u_{\mathrm{ref\_wj\_left}}(i)$, $u_{\mathrm{ref\_wj\_right}}(i)$, and $u_{\mathrm{ref\_uj\_left}}(i)$, $u_{\mathrm{ref\_uj\_right}}(i)$), which can be proved by the simulation results in Section IV and the experimental results in Section V. Therefore, the assumption is reasonable. Moreover, the capacitance of the SM is usually designed to limit the voltage fluctuations of the SMs within 10% of the rated capacitor voltages. So the capacitor voltage fluctuations are ignored in the following analysis for simplicity.

Based on the double-Fourier analysis [40], the output voltages of *H* HBSMs and *F* FBSMs in the lower arm can be given by

$$\begin{aligned} u_{\mathrm{whj}} =\ & \frac{HV_{\mathrm{dc}}}{2N} + \frac{HMV_{\mathrm{dc}}}{2N}\cos(\omega_o t+\varphi_j) \\ & + \sum_{m=1}^{\infty}\sum_{n=-\infty}^{\infty} \frac{2V_{\mathrm{dc}}}{m\pi N} \\ & \times \sin\left[\frac{(Hm+n)\pi}{2}\right] \times J_n\left(\frac{MHm\pi}{2}\right) \\ & \times \cos\left[Hm\omega_c t + n(\omega_o t+\varphi_j)\right] \end{aligned} \tag{15}$$

$$\begin{aligned} u_{\mathrm{wfj}} =\ & \frac{FV_{\mathrm{dc}}}{2N} + \frac{FMV_{\mathrm{dc}}}{2N}\cos(\omega_o t+\varphi_j) \\ & + \sum_{m=1}^{\infty}\sum_{n=-\infty}^{\infty} \frac{(-1)^{Fm+n}2V_{\mathrm{dc}}}{m\pi N} \\ & \times J_{2n+1-Fm}\left(\frac{MFm\pi}{2}\right) \\ & \times \cos\left[2Fm\omega_c t + (2n+1-Fm)(\omega_o t+\varphi_j)\right] \end{aligned} \tag{16}$$

where $m\,(m=1,\ldots,\infty)$ is the harmonic order of the carrier wave, $n\,(n=-\infty,\ldots,-1,0,1\ldots,\infty)$ is the harmonic order of the reference wave, $J_n\,(x)$ is the Bessel coefficient of order n and argument x, and ω_c is the angular frequency of the triangular carriers.

The lower arm output voltage is expressed as

$$\begin{aligned} u_{\mathrm{wj}} =\ & u_{\mathrm{whj}} + u_{\mathrm{wfj}} = \frac{V_{\mathrm{dc}}}{2} + \frac{MV_{\mathrm{dc}}}{2} cos(\omega_o t+\varphi_j) \\ & + \sum_{m=1}^{\infty}\sum_{n=-\infty}^{\infty} \frac{2V_{\mathrm{dc}}}{m\pi N} \times \sin\left[\frac{(Hm+n)\pi}{2}\right] \\ & \times J_n\left(\frac{MHm\pi}{2}\right) \times \cos\left[Hm\omega_c t + n(\omega_o t+\varphi_j)\right] \\ & + \sum_{m=1}^{\infty}\sum_{n=-\infty}^{\infty} \frac{(-1)^{Fm+n}2V_{\mathrm{dc}}}{m\pi N} \times J_{2n+1-Fm}\left(\frac{MFm\pi}{2}\right) \\ & \times \cos\left[2Fm\omega_c t + (2n+1-Fm)(\omega_o t+\varphi_j)\right]. \end{aligned} \tag{17}$$

Similarly, the output voltage of the upper arm is expressed as

$$\begin{aligned} u_{\mathrm{uj}} =\ & \frac{V_{\mathrm{dc}}}{2} - \frac{MV_{\mathrm{dc}}}{2}\cos(\omega_o t+\varphi_j) \\ & + \sum_{m=1}^{\infty}\sum_{n=-\infty}^{\infty} \frac{2V_{\mathrm{dc}}}{m\pi N} \times \sin\left[\frac{(Hm+n)\pi}{2}\right] \times J_n\left(\frac{MHm\pi}{2}\right) \\ & \times \cos\left[Hm(\omega_c t+\theta) + n(\omega_o t+\varphi_j+\pi)\right] \\ & + \sum_{m=1}^{\infty}\sum_{n=-\infty}^{\infty} \frac{(-1)^{Fm+n}2V_{\mathrm{dc}}}{m\pi N} \times J_{2n+1-Fm}\left(\frac{MFm\pi}{2}\right) \\ & \times \cos\left[2Fm(\omega_c t+\theta) + (2n+1-Fm)(\omega_o t+\varphi_j+\pi)\right]. \end{aligned} \tag{18}$$

Therefore, the output phase voltage and the circulating current of phase j can be derived by following the similar derivation process given in [40] and they can be expressed as

$$\begin{aligned} u_{\mathrm{oj}} =\ & \frac{MV_{\mathrm{dc}}}{2}\cos(\omega_o t+\varphi_j) + \sum_{m=1}^{\infty}\sum_{n=-\infty}^{\infty} \frac{(-1)^n 2V_{\mathrm{dc}}}{m\pi N} \\ & \times J_{2n+1-Hm}\left(\frac{MHm\pi}{2}\right) \\ & \times \cos\left[Hm\omega_c t + (2n+1-Hm)(\omega_o t+\varphi_j)\right. \\ & \left. + \frac{Hm(\theta_h-\pi)}{2}\right] \times \cos\left[\frac{Hm(\theta_h-\pi)}{2}\right] \\ & + \sum_{m=1}^{\infty}\sum_{n=-\infty}^{\infty} \frac{(-1)^{Fm+n}2V_{\mathrm{dc}}}{m\pi N} \\ & \times J_{2n+1-Fm}\left(\frac{MFm\pi}{2}\right) \\ & \times \cos\left[2Fm\omega_c + (2n+1-Fm)(\omega_o t+\varphi_j)\right. \\ & \left. + Fm\left(\theta_f-\frac{\pi}{2}\right)\right] \times \cos\left[Fm\left(\theta_f-\frac{\pi}{2}\right)\right] \end{aligned} \tag{19}$$

$$\begin{aligned} i_{\mathrm{cj}} =\ & \frac{I_{\mathrm{dc}}}{3} + \sum_{m=1}^{\infty}\sum_{n=-\infty}^{\infty} \frac{(-1)^n V_{\mathrm{dc}}}{m\pi N L_0(Hm\omega_c + (2n+1-Hm)\omega_o)} \\ & \times J_{2n+1-Hm}\left(\frac{MHm\pi}{2}\right) \\ & \times \cos\left(Hm\omega_c t + (2n+1-Hm)(\omega_o t+\varphi_j)\right. \\ & \left. + \frac{Hm(\theta_h-\pi)}{2}\right) \times \sin\left(\frac{Hm(\theta_h-\pi)}{2}\right) \\ & + \sum_{m=1}^{\infty}\sum_{n=-\infty}^{\infty} \frac{(-1)^{Fm+n}V_{\mathrm{dc}}}{m\pi N L_0(2Fm\omega_c + (2n+1-Fm)w_o)} \\ & \times J_{2n+1-Fm}\left(\frac{MFm\pi}{2}\right) \\ & \times \cos\left(2Fm\omega_c t + (2n+1-Fm)(\omega_o t+\varphi_j)\right. \end{aligned}$$

$$+Fm\left(\theta_f-\frac{\pi}{2}\right)\Bigg)\times\sin\left(Fm\left(\theta_f-\frac{\pi}{2}\right)\right). \tag{20}$$

The second term in (19) is the voltage harmonics generated by the HBSMs, while the third term is the voltage harmonics generated by the FBSMs. When these two terms are minimized simultaneously by properly choosing the displacement angles θ_h and θ_f, the output voltage harmonics minimization can be achieved. Similarly, the circulating current harmonics cancellation can be achieved when the second term and the third term in (20) are equal to zero simultaneously.

The output voltage harmonics minimization can be achieved in the hybrid MMC by choosing the displacement angle as follows:

$$\begin{cases}\theta_h=0, & H \text{ is odd}\\ \theta_h=\dfrac{\pi}{H}, & H \text{ is even}\end{cases}\text{ and }\begin{cases}\theta_f=0, & F \text{ is odd}\\ \theta_f=\dfrac{\pi}{2F}, & F \text{ is even}\end{cases}. \tag{21}$$

Under this condition, (22) and (23) shown at the bottom of the page can be easily deduced.

It can be seen that the voltage harmonics at odd multiples of the *Hm*th carrier group and the *Fm*th carrier group will be zero. Then, the output phase voltage is derived as

$$\begin{aligned}u_{\mathrm{oj}}=&\frac{MV_{\mathrm{dc}}}{2}\cos(\omega_o t+\varphi_j)+\sum_{m=1}^{\infty}\sum_{n=-\infty}^{\infty}\frac{(-1)^{n+1}V_{\mathrm{dc}}}{m\pi N}\\&\times J_{2n+1-2Hm}\left(MHm\pi\right)\\&\times\cos\left[2Hm\omega_c t+(2n+1-2Hm)(\omega_o t+\varphi_j)\right]\\&+\sum_{m=1}^{\infty}\sum_{n=-\infty}^{\infty}\frac{(-1)^{Fm+n+1}V_{\mathrm{dc}}}{m\pi N}\\&\times J_{2n+1-2Fm}\left(MFm\pi\right)\\&\times\cos\left[4Fm\omega_c+(2n+1-2Fm)(\omega_o t+\varphi_j)\right].\end{aligned} \tag{24}$$

Due to the fact that the voltage harmonics at odd multiples of the *Hm*th carrier group and the *Fm*th carrier group are zero, the center frequency of the lowest harmonic group is $2Hf_{\mathrm{c}}$. Since the number of HBSMs is less than FBSMs ($H \le F \le N$) in the hybrid MMC in order to provide dc-side short-circuit protection, the center frequency of the lowest harmonic group is even lower than that of the HBSMs-based MMC ($2Hf_{\mathrm{c}} \le Nf_{\mathrm{c}}$). The center frequency of the lowest harmonic group for the circulating current is Hf_{c} because the odd multiples of the *Hm*th carrier group harmonics in the circulating current cannot be cancelled at this displacement angle.

The circulating current harmonics cancellation can be achieved in the hybrid MMC by choosing the displacement angle as follows:

$$\begin{cases}\theta_h=\dfrac{\pi}{H}, & H \text{ is odd}\\ \theta_h=0, & H \text{ is even}\end{cases}\text{ and }\begin{cases}\theta_f=\dfrac{\pi}{2F}, & F \text{ is odd}\\ \theta_f=0, & F \text{ is even}\end{cases}. \tag{25}$$

Under this condition, the following equations can be easily obtained:

$$\sin\left(\frac{Hm(\theta_h-\pi)}{2}\right)=\begin{cases}\sin\left(\frac{m\pi(1-H)}{2}\right)=0, & H \text{ is odd}\\ \sin\left(\frac{Hm\pi}{2}\right)=0, & H \text{ is even}\end{cases} \tag{26}$$

$$\sin\left(Fm\left(\theta_f-\frac{\pi}{2}\right)\right)=\begin{cases}\sin\left(\frac{m\pi(1-F)}{2}\right)=0, & F \text{ is odd}\\ \sin\left(\frac{Fm\pi}{2}\right)=0, & F \text{ is even}\end{cases}. \tag{27}$$

Therefore, the second term and the third term in (16) are always equal to zero, so the circulating current switching harmonics can be fully cancelled. A pure circulating current without undesirable switching harmonics can be achieved, thus the dc filters can be avoided. The center frequency of the lowest harmonic group for the output voltage is Hf_{c} because the odd multiples of the *Hm*th carrier group harmonics in the output voltage cannot be cancelled at this displacement angle. From (21) and (25), it is clear that the output voltage harmonics minimization and the circulating current harmonics cancellation cannot be achieved at the same time.

It can be seen that the center frequency of the output voltage lowest harmonic group is limited by the number of the HBSMs if the traditional PSC-PWM scheme is directly used in the hybrid MMC. The cutoff frequency of the output filter is low due to the low center frequency of the lowest harmonic group, so the filter size is inevitably enlarged in order to attenuate these harmonics. Another issue is that the number of power devices of the FBSM is double the number of the HBSM. The same carrier frequency is employed for the HBSM and the FBSM,

$$\cos\left(\frac{Hm(\theta_h-\pi)}{2}\right)=\begin{cases}\cos\left(\dfrac{Hm\pi}{2}\right)=\begin{cases}0, & Hm \text{ is odd}\\ 1 \text{ or } (-1), & Hm \text{ is even}\end{cases}, & H \text{ is odd}\\ \cos\left(\dfrac{m\pi(1-H)}{2}\right)=\begin{cases}0, & Hm \text{ is odd}\\ 1 \text{ or } (-1), & Hm \text{ is even}\end{cases}, & H \text{ is even}\end{cases} \tag{22}$$

$$\cos\left(Fm\left(\theta_f-\frac{\pi}{2}\right)\right)=\begin{cases}\cos\left(\dfrac{Fm\pi}{2}\right)=\begin{cases}0, & Fm \text{ is odd}\\ 1 \text{ or } (-1), & Fm \text{ is even}\end{cases}, & F \text{ is odd}\\ \cos\left(\dfrac{m\pi(1-F)}{2}\right)=\begin{cases}0, & Fm \text{ is odd}\\ 1 \text{ or} (-1), & Fm \text{ is even}\end{cases}, & F \text{ is even}\end{cases}. \tag{23}$$

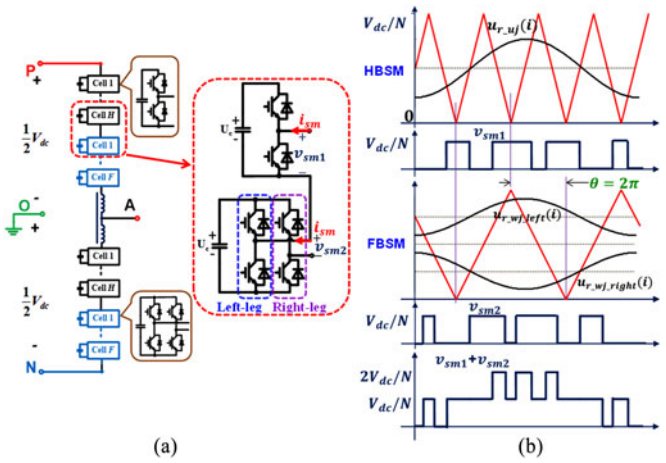

Fig. 6. Output voltage of hybrid arm composed of single HBSM and single FBSM with improved PSC-PWM scheme.

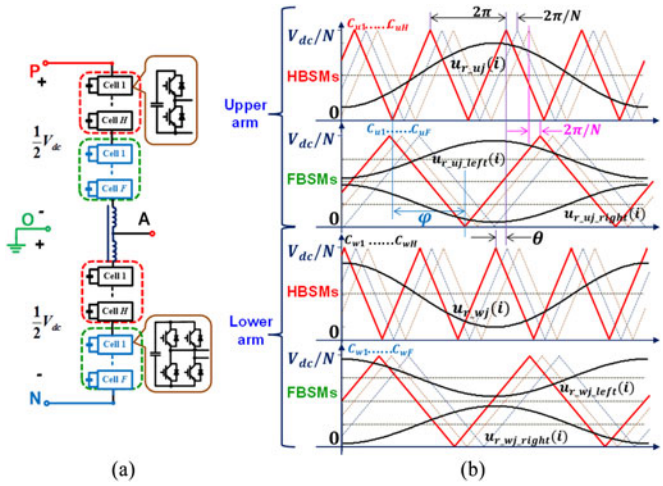

Fig. 7. Improved PSC-PWM scheme for a hybrid MMC.

so the total switching loss of the FBSM is also double that of the HBSM, which induces significantly uneven loss distribution between the HBSMs and the FBSMs.

B. Improved PSC-PWM Scheme for Hybrid MMC

To deal with the issues associated with the traditional PSC-PWM scheme in the hybrid MMC, an improved PSC-PWM scheme is proposed. Take the combination of single HBSM and single FBSM in the hybrid arm, as an example, which is shown in Fig. 6. The switching frequency of the FBSM is reduced to half that of the HBSM, so the output equivalent switching frequencies of the FBSM and the HBSM are the same. The total switching loss of the FBSM is close to the HBSM, which alleviates the uneven loss distribution between the HBSMs and the FBSMs. In addition, a proper phase-shifting angle θ, which is equal to 2π, in this case, is employed between the HBSM and the FBSM in order to achieve the best harmonic cancellation effect. Then, the mismatch pulses on the output voltage are eliminated as shown in Fig. 6(b).

The improved PSC-PWM scheme for the hybrid MMC is shown in Fig. 7. The triangular carriers of H HBSMs and F FBSMs in each arm are shifted by $2\pi/N$ and a phase-shifting angle $\varphi\,(0 \le \varphi \le 2\pi)$ is applied between the HBSMs and the FBSMs. Accordingly, the modulation signal distribution of the improved PSC-PWM for the hybrid MMC is shown in Fig. 8.

Based on the double-Fourier analysis [40], the Fourier representation of the output voltages of ith HBSM and ith FBSM in the lower arm, $u_{\mathrm{whj}}\,(i)$, $u_{\mathrm{wfj}}\,(i)$ can be expressed as

$$u_{\mathrm{whj}}(i) = \frac{V_{\mathrm{dc}}}{2N} + \frac{MV_{\mathrm{dc}}}{2N}\cos(\omega_o t + \varphi_j) + \sum_{m=1}^{\infty}\sum_{n=-\infty}^{\infty}\frac{2V_{\mathrm{dc}}}{m\pi N} \times \sin\left[\frac{(m+n)\pi}{2}\right] \times J_n\left(\frac{Mm\pi}{2}\right) \times \cos\left[m\left(\omega_{\mathrm{ch}}t + (i-1)\frac{2\pi}{N}\right) + n(\omega_o t + \varphi_j)\right] \quad (28)$$

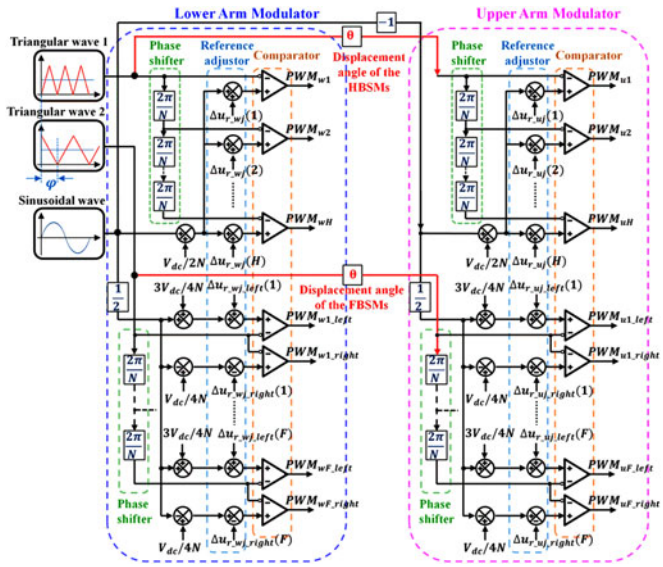

Fig. 8. Modulation signals distribution of improved PSC-PWM for a hybrid MMC.

$$u_{\mathrm{wfj}}(i) = \frac{V_{\mathrm{dc}}}{2N} + \frac{MV_{\mathrm{dc}}}{2N}\cos(\omega_o t + \varphi_j) + \sum_{m=1}^{\infty}\sum_{n=-\infty}^{\infty}\frac{V_{\mathrm{dc}}}{m\pi N} \times J_n\left(\frac{Mm\pi}{2}\right) \times \cos\left[2m\left(\omega_{\mathrm{cf}}t + \frac{\varphi}{2} + (i-1)\frac{\pi}{N}\right) + n(\omega_o t + \varphi_j)\right] \times \left\{\sin\left[(3m+n)\frac{\pi}{2}\right] - (-1)^n \sin\left[(m+n)\frac{\pi}{2}\right]\right\} \quad (29)$$

where ω_{ch} is the angular frequency of the HBSM triangular carriers, and ω_{cf} is the angular frequency of the FBSM triangular carriers. Note the phase-shifting angle φ becomes $\varphi_f\ \left(\varphi_f = \frac{\varphi}{2}\right)$ in (29) because the carrier frequency of the FBSM is half that of the HBSM.

The Fourier representation of the output voltages of *i*th HBSM and *i*th FBSM in the upper arm, $u_{\mathrm{uhj}}(i)$ and $u_{\mathrm{ufj}}(i)$ can be expressed as

$$\begin{aligned} u_{\mathrm{uhj}}(i) = {} & \frac{V_{\mathrm{dc}}}{2N} + \frac{MV_{\mathrm{dc}}}{2N}\cos(\omega_o t + \varphi_j) \\ & + \sum_{m=1}^{\infty}\sum_{n=-\infty}^{\infty} \frac{2V_{\mathrm{dc}}}{m\pi N} \times \sin\left[\frac{(m+n)\pi}{2}\right] \times J_n\left(\frac{Mm\pi}{2}\right) \\ & \times \cos\left[m\left(\omega_{\mathrm{ch}} t + \theta + (i-1)\frac{2\pi}{N}\right)\right. \\ & \left. + n(\omega_o t + \varphi_j + \pi)\right] \end{aligned} \tag{30}$$

$$\begin{aligned} u_{\mathrm{ufj}}(i) = {} & \frac{V_{\mathrm{dc}}}{2N} + \frac{MV_{\mathrm{dc}}}{2N}\cos(\omega_o t + \varphi_j) + \sum_{m=1}^{\infty}\sum_{n=-\infty}^{\infty} \frac{V_{\mathrm{dc}}}{m\pi N} \\ & \times J_n\left(\frac{Mm\pi}{2}\right) \times \cos\left[2m\left(\omega_{\mathrm{cf}} t + \frac{\varphi}{2} + \frac{\theta}{2} + (i-1)\frac{\pi}{N}\right)\right. \\ & \left. + n(\omega_o t + \varphi_j + \pi)\right] \\ & \times \left\{\sin\left[(3m+n)\frac{\pi}{2}\right] - (-1)^n \sin\left[(m+n)\frac{\pi}{2}\right]\right\}. \end{aligned} \tag{31}$$

Note the displacement angle θ becomes θ_f $\left(\theta_f = \frac{\theta}{2}\right)$ in (31) because the carrier frequency of the FBSM is half that of the HBSM. Because $\omega_{\mathrm{ch}} = 2\omega_{\mathrm{cf}}$, (29) and (31) can be derived as

$$\begin{aligned} u_{\mathrm{wfj}}(i) = {} & \frac{V_{\mathrm{dc}}}{2N} + \frac{MV_{\mathrm{dc}}}{2N}\cos(\omega_o t + \varphi_j) + \sum_{m=1}^{\infty}\sum_{n=-\infty}^{\infty} \frac{2V_{\mathrm{dc}}}{m\pi N} \\ & \times J_n\left(\frac{Mm\pi}{2}\right) \\ & \times \cos\left[m\left(\omega_{\mathrm{ch}} t + \varphi + (i-1)\frac{2\pi}{N}\right) + n(\omega_o t + \varphi_j)\right] \\ & \times \frac{1}{2}\left\{\sin\left[(3m+n)\frac{\pi}{2}\right]\right. \\ & \left. - (-1)^n \sin\left[(m+n)\frac{\pi}{2}\right]\right\} \end{aligned} \tag{32}$$

$$\begin{aligned} u_{\mathrm{ufj}}(i) = {} & \frac{V_{\mathrm{dc}}}{2N} + \frac{MV_{\mathrm{dc}}}{2N}\cos(\omega_o t + \varphi_j) + \sum_{m=1}^{\infty}\sum_{n=-\infty}^{\infty} \frac{2V_{\mathrm{dc}}}{m\pi N} \\ & \times J_n\left(\frac{Mm\pi}{2}\right) \times \cos\left[m\left(\omega_{\mathrm{ch}} t + \varphi + \theta + (i-1)\frac{2\pi}{N}\right)\right. \\ & \left. + n(\omega_o t + \varphi_j + \pi)\right] \\ & \times \frac{1}{2}\left\{\sin\left[(3m+n)\frac{\pi}{2}\right] - (-1)^n \sin\left[(m+n)\frac{\pi}{2}\right]\right\}. \end{aligned} \tag{33}$$

By summing the output voltages of the *H* HBSMs and the *F* FBSMs, the arm voltages can be obtained as

$$\begin{aligned} u_{\mathrm{wj}} = {} & \sum_{i=1}^{H} u_{\mathrm{whj}}(i) + \sum_{i=1}^{F} u_{\mathrm{wfj}}(i) = \frac{V_{\mathrm{dc}}}{2} + \frac{MV_{\mathrm{dc}}}{2}\cos(\omega_o t + \varphi_j) \\ & + \sum_{m=1}^{\infty}\sum_{n=-\infty}^{\infty} \frac{2V_{\mathrm{dc}}}{m\pi N} \times J_n\left(\frac{Mm\pi}{2}\right) \times \sin\left[\frac{(m+n)\pi}{2}\right] \\ & \times \left\{\sum_{i=1}^{H} \cos\left[m\left(\omega_{\mathrm{ch}} t + (i-1)\frac{2\pi}{N}\right) + n(\omega_o t + \varphi_j)\right]\right. \\ & \left. + \sum_{i=1}^{F} \begin{array}{l} \cos\left[m\left(\omega_{\mathrm{ch}} t + \varphi + (i-1)\frac{2\pi}{N}\right) + n(\omega_o t + \varphi_j)\right] \\ \times \frac{1}{2}\left[(-1)^m - (-1)^n\right] \end{array}\right\} \end{aligned} \tag{34}$$

$$\begin{aligned} u_{\mathrm{uj}} = {} & \sum_{i=1}^{H} u_{\mathrm{uhj}}(i) + \sum_{i=1}^{F} u_{\mathrm{ufj}}(i) = \frac{V_{\mathrm{dc}}}{2} + \frac{MV_{\mathrm{dc}}}{2}\cos(\omega_o t + \varphi_j) \\ & + \sum_{m=1}^{\infty}\sum_{n=-\infty}^{\infty} \frac{2V_{\mathrm{dc}}}{m\pi N} \times J_n\left(\frac{Mm\pi}{2}\right) \times \sin\left[\frac{(m+n)\pi}{2}\right] \\ & \times \left\{\sum_{i=1}^{H} \cos\left[m\left(\omega_{\mathrm{ch}} t + \theta + (i-1)\frac{2\pi}{N}\right)\right.\right. \\ & \left. + n(\omega_o t + \varphi_j + \pi)\right] \\ & \left. + \sum_{i=1}^{F} \begin{array}{l} \cos\left[m\left(\omega_{\mathrm{ch}} t + \varphi + \theta + (i-1)\frac{2\pi}{N}\right)\right. \\ \left. + n(\omega_o t + \varphi_j + \pi)\right] \\ \times \frac{1}{2}\left[(-1)^m - (-1)^n\right]. \end{array}\right\} \end{aligned} \tag{35}$$

To achieve the best harmonic cancellation effect, the FBSMs should behave like the HBSMs with phase shifted by $2\pi/N$ incrementally [43]. Therefore, the term $\sum_{i=1}^{F} \cos\left[m\left(\omega_{\mathrm{ch}} t + \varphi + (i-1)\frac{2\pi}{N} +\right) + n(\omega_o t + \varphi_j)\right] \times \frac{1}{2}\left[(-1)^m - (-1)^n\right]$ in (34) should satisfy

$$\begin{aligned} & \sum_{i=1}^{F} \begin{array}{l} \cos\left[m\left(\omega_{\mathrm{ch}} t + \varphi + (i-1)\frac{2\pi}{N} +\right) + n(\omega_o t + \varphi_j)\right] \\ \times \frac{1}{2}\left[(-1)^m - (-1)^n\right] \end{array} \\ & = \sum_{i=H+1}^{N} \cos\left[m\left(\omega_{\mathrm{ch}} t + (i-1)\frac{2\pi}{N}\right) + n(\omega_o t + \varphi_j)\right]. \end{aligned} \tag{36}$$

Assuming $\varphi = a\pi + b\,(0 \le \varphi \le 2\pi)$, due to $H + F = N$, the following equation can be obtained:

$$\begin{aligned} & \sum_{i=1}^{F} \cos\left[m\left(\omega_{\mathrm{ch}} t + \varphi + (i-1)\frac{2\pi}{N}\right) + n(\omega_o t + \varphi_j)\right] \\ & \quad \times \frac{1}{2}\left[(-1)^m - (-1)^n\right] \\ & = \sum_{i=H+1}^{N} \cos\left[m\left(\omega_{\mathrm{ch}} t + (i-1)\frac{2\pi}{N} - \frac{2\pi H}{N} + b\right)\right. \end{aligned}$$

$$+ n(\omega_o t + \varphi_j)\Big]\frac{1}{2}\left[(-1)^{m+\mathrm{am}} - (-1)^{n+\mathrm{am}}\right] = \sum_{i=H+1}^{N} \cos\left[m\left(\omega_{\mathrm{ch}} t + (i-1)\frac{2\pi}{N}\right) + n(\omega_o t + \varphi_j)\right]. \tag{37}$$

So the following equation can be derived:

$$\begin{cases} \frac{1}{2}\left[(-1)^{m+\mathrm{am}} - (-1)^{n+\mathrm{am}}\right] = 1 \\ b - \frac{2\pi H}{N} = 0. \end{cases} \tag{38}$$

If $(m + n)$ is even, the third terms in (34) and (35) become zero. Therefore, (38) should be satisfied when $(m + n)$ is odd. The values of a and b can be obtained as

$$\begin{cases} a = 1 \\ b = \frac{2\pi H}{N}. \end{cases} \tag{39}$$

Then, phase-shifting angle φ is given by

$$\varphi = \pi + \frac{2\pi H}{N}. \tag{40}$$

Note this phase-shifting angle is based on the carrier frequency of the HBSM.

Therefore, (34) and (35) can be rewritten as

$$u_{\mathrm{wj}} = \sum_{i=1}^{H} u_{\mathrm{whj}}(i) + \sum_{i=1}^{F} u_{\mathrm{wfj}}(i) = \frac{V_{\mathrm{dc}}}{2} + \frac{MV_{\mathrm{dc}}}{2}\cos(\omega_o t + \varphi_j) + \sum_{m=1}^{\infty}\sum_{n=-\infty}^{\infty} \frac{2V_{\mathrm{dc}}}{m\pi N} \times J_n\left(\frac{Mm\pi}{2}\right) \times \sin\left[\frac{(m+n)\pi}{2}\right] \times \left\{\sum_{i=1}^{H} \cos\left[m\left(\omega_{\mathrm{ch}} t + (i-1)\frac{2\pi}{N}\right) + n(\omega_o t + \varphi_j)\right] + \sum_{i=1}^{F} \cos\left[m\left(\omega_{\mathrm{ch}} t + \frac{2\pi H}{N} + (i-1)\frac{2\pi}{N}\right) + n(\omega_o t + \varphi_j)\right]\right\} \tag{41}$$

$$u_{\mathrm{uj}} = \sum_{i=1}^{H} u_{\mathrm{uhj}}(i) + \sum_{i=1}^{F} u_{\mathrm{ufj}}(i) = \frac{V_{\mathrm{dc}}}{2} + \frac{MV_{\mathrm{dc}}}{2}\cos(\omega_o t + \varphi_j) + \sum_{m=1}^{\infty}\sum_{n=-\infty}^{\infty} \frac{2V_{\mathrm{dc}}}{m\pi N} \times J_n\left(\frac{Mm\pi}{2}\right) \times \sin\left[\frac{(m+n)\pi}{2}\right] \times \left\{\sum_{i=1}^{H} \cos\left[m\left(\omega_{\mathrm{ch}} t + \theta + (i-1)\frac{2\pi}{N}\right) + n(\omega_o t + \varphi_j + \pi)\right] + \sum_{i=1}^{F} \cos\left[m\left(\omega_{\mathrm{ch}} t + \theta + \frac{2\pi H}{N} + (i-1)\frac{2\pi}{N}\right) + n(\omega_o t + \varphi_j + \pi)\right]\right\}. \tag{42}$$

Then, the following equations can be derived:

$$u_{\mathrm{wj}} = \frac{V_{\mathrm{dc}}}{2} + \frac{MV_{\mathrm{dc}}}{2}\cos(\omega_o t + \varphi_j) + \sum_{m=1}^{\infty}\sum_{n=-\infty}^{\infty} \frac{2V_{\mathrm{dc}}}{m\pi N} \times J_n\left(\frac{Mm\pi}{2}\right) \times \sin\left[\frac{(m+n)\pi}{2}\right] \times \left\{\sum_{i=1}^{N} \cos\left[m\left(\omega_{\mathrm{ch}} t + (i-1)\frac{2\pi}{N}\right) + n(\omega_o t + \varphi_j)\right]\right\} \tag{43}$$

$$u_{\mathrm{uj}} = \frac{V_{\mathrm{dc}}}{2} + \frac{MV_{\mathrm{dc}}}{2}\cos(\omega_o t + \varphi_j) + \sum_{m=1}^{\infty}\sum_{n=-\infty}^{\infty} \frac{2V_{\mathrm{dc}}}{m\pi N} \times J_n\left(\frac{Mm\pi}{2}\right) \times \sin\left[\frac{(m+n)\pi}{2}\right] \times \left\{\sum_{i=1}^{N} \cos\left[m\left(\omega_{\mathrm{ch}} t + \theta + (i-1)\frac{2\pi}{N}\right) + n(\omega_o t + \varphi_j + \pi)\right]\right\}. \tag{44}$$

According to the derivation process given in [40], the output voltage and the circulating current of phase j can be obtained as follows:

$$u_{\mathrm{oj}} = \frac{MV_{\mathrm{dc}}}{2}\cos(\omega_o t + \varphi_j) + \sum_{m=1}^{\infty}\sum_{n=-\infty}^{\infty} \frac{(-1)^n 2V_{\mathrm{dc}}}{m\pi N} \times J_{2n+1-Nm}\left(\frac{MNm\pi}{2}\right) \times \cos\left(Nm\omega_{\mathrm{ch}} t + (2n+1-Nm)(\omega_o t + \varphi_j) + \frac{Nm(\theta-\pi)}{2}\right)\cos\left(\frac{Nm(\theta-\pi)}{2}\right) \tag{45}$$

$$i_{\mathrm{cj}} = \frac{I_{\mathrm{dc}}}{3} + \sum_{m=1}^{\infty}\sum_{n=-\infty}^{\infty} \frac{(-1)^n V_{\mathrm{dc}}}{m\pi N L_0(Nm\omega_{\mathrm{ch}} + (2n+1-Nm)\omega_o)} \times J_{2n+1-Nm}\left(\frac{MNm\pi}{2}\right) \times \cos\left(Nm\omega_{\mathrm{ch}} t + (2n+1-Nm)(\omega_o t + \varphi_j) + \frac{Nm(\theta-\pi)}{2}\right) \times \sin\left(\frac{Nm(\theta-\pi)}{2}\right). \tag{46}$$

The output voltage harmonics minimization can be achieved in the hybrid MMC by choosing the displacement angle as follows:

$$\theta = \begin{cases} 0, & N \text{ is odd} \\ \frac{\pi}{N}, & N \text{ is even} \end{cases}. \tag{47}$$

Under this condition, the following equations can be easily deduced:

$$\cos\left(\frac{Nm(\theta-\pi)}{2}\right) = \begin{cases} \cos\left(\frac{Nm\pi}{2}\right) = \begin{cases} 0, & Nm \text{ is odd} \\ 1 \text{ or } (-1), & Nm \text{ is even} \end{cases}, & N \text{ is odd} \\ \cos\left(\frac{m\pi(1-N)}{2}\right) = \begin{cases} 0, & Nm \text{ is odd} \\ 1 \text{ or } (-1), & Nm \text{ is even} \end{cases}, & N \text{ is even.} \end{cases} \tag{48}$$

It can be seen that the voltage harmonics at odd multiples of the *Nm*th carrier group are zero. Then, the output phase voltage is derived as

$$\begin{aligned} u_{\mathrm{oj}} = & \frac{MV_{\mathrm{dc}}}{2}\cos(\omega_o t+\varphi_j) + \sum_{m=1}^{\infty}\sum_{n=-\infty}^{\infty}\frac{(-1)^{n+1}V_{\mathrm{dc}}}{m\pi N} \\ & \times J_{2n+1-2Nm}\left(MNm\pi\right) \\ & \times\cos\left[2Nm\omega_{\mathrm{ch}}t+(2n+1-2Nm)(\omega_o t+\varphi_j)\right]. \end{aligned} \tag{49}$$

Due to the fact that voltage harmonics at odd multiples of the *Nm*th carrier group are zero, the center frequency of the lowest harmonic group is $2Nf_{\mathrm{ch}}$. Therefore, the filter size can be significantly reduced because the cutoff frequency of the output filter is at least doubled compared with the traditional PSC-PWM scheme for the hybrid MMC. The center frequency of the lowest harmonic group for the circulating current is Nf_{ch} because the odd multiples of the *Nm*th carrier group harmonics in the circulating current cannot be cancelled at this displacement angle.

The circulating current harmonics cancellation can be achieved in the hybrid MMC by choosing the displacement angle as follows:

$$\theta = \begin{cases} \dfrac{\pi}{N}, & N \text{ is odd} \\ 0, & N \text{ is even} \end{cases}. \tag{50}$$

Under this condition, the following equation can be easily obtained:

$$\sin\left(\frac{Nm(\theta-\pi)}{2}\right) = \begin{cases} \sin\left(\frac{m\pi(1-N)}{2}\right)=0, & N \text{ is odd} \\ \sin\left(\frac{Nm\pi}{2}\right)=0, & N \text{ is even} \end{cases}. \tag{51}$$

Therefore, the second term in (46) is always equal to zero, so the circulating current switching harmonics are fully cancelled. A pure circulating current without undesirable switching harmonics can be achieved, so the dc-side filters can be avoided. The center frequency of the lowest harmonic group for the output voltage is Nf_{ch} because the odd multiples of the *Nm*th carrier group harmonics in the output voltage cannot be cancelled at this displacement angle. From (47) and (50), it is clear that the output voltage harmonics minimization and the circulating current harmonics cancellation cannot be achieved at the same time.

The improved PSC-PWM scheme increases the center frequency of the output voltage lowest harmonic group to $2Nf_{\mathrm{ch}}$, which is at least double that of the traditional PSC-PWM scheme for the hybrid MMC. In addition, the improved PSC-PWM scheme employs lower switching frequency for the FBSMs, which can alleviate the uneven loss distribution between the HBSMs and the FBSMs and reduce the total switching loss of the system.

TABLE I
PARAMETERS OF THE SIMULATION

Parameters	Values	Parameters	Values
Rated active power P	1 MW	SM Capacitance C	1.9 mF
DC-link voltage V_{dc}	9 kV	Unit capacitance constant [44] H	77 ms
Rated line-to-line rms voltage V_{ll}	4.5 kV (rms)	Carrier frequency f_{c}	750 Hz
Number of SMs per arm N	6	Carrier frequency for HBSMs f_{ch}	750 Hz
Number of HBSMs per arm H	3	Carrier frequency for FBSMs f_{cf}	375 Hz
Number of FBSMs per arm F	3	Fundamental frequency f_0	50 Hz
Arm inductance $L_{\mathrm{u}} = L_{\mathrm{w}} = M = L_{\mathrm{o}}$	1 mH (1.6%)	Load inductance L_{Load}	1.7 mH (2.6%)
Rated SM Capacitor voltage U_{c}	1.5 kV	Output ac current	128 A (rms)

Values in () are on a three-phase 4.5-kV, 1-MW, and 50-Hz base.

IV. SIMULATED RESULTS

In order to verify the theoretical analysis and the validity of the improved PSC-PWM scheme, a simulation model of the hybrid MMC is built in the MATLAB/Simulink and the structure of the simulation model is shown in Fig. 1. Each arm contains three HBSMs and three FBSMs. The coupled inductors are employed as the arm inductors and the resistive loads are used in the simulation. The parameters of the simulation model are tabulated in Table I. The carrier frequency for the HBSMs and the FBSMs under the traditional PSC-PWM scheme is 750 Hz. The carrier frequencies for the HBSMs and the FBSMs under the improved PSC-PWM scheme are 750 and 375 Hz, respectively.

A. Hybrid MMC With Traditional PSC-PWM Scheme

The simulated results of the hybrid MMC with the traditional PSC-PWM scheme are shown in Figs. 9–14. Figs. 9 and 10 show the simulated results of the hybrid MMC using the traditional PSC-PWM scheme for the circulating current harmonics cancellation. Fig. 9 shows the phase voltage u_{oa} and the circulating current waveform i_{ca}. Fig. 10 shows the capacitors voltages, the arm currents, and the output current waveform.

It can be seen that there are some mismatch pulses on the phase voltage u_{oa} as shown in Fig. 9(a) due to the different output equivalent switching frequencies of the HBSMs and the FBSMs. The center frequency of the lowest harmonic group of the phase voltage is 2250 Hz ($3f_{\mathrm{c}} = 3^{*}750$ Hz) as shown in Fig. 11(a), which is equal to Hf_{c} as presented in Section III-A.

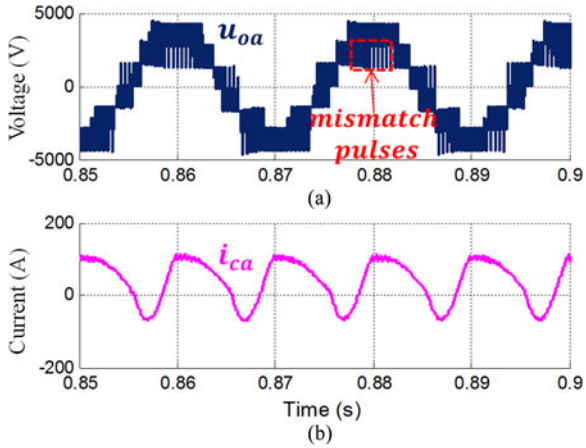

Fig. 9. Simulated waveforms of hybrid MMC using traditional PSC-PWM scheme for circulating current harmonics cancellation. (a) Phase voltage u_{oa} and (b) circulating current i_{ca}.

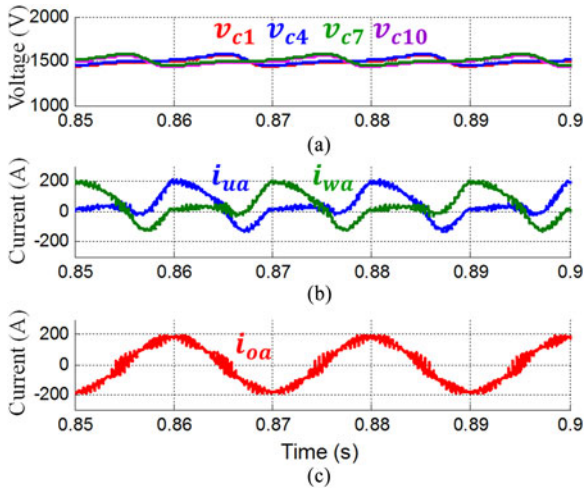

Fig. 10. Simulated waveforms of hybrid MMC using traditional PSC-PWM scheme for circulating current harmonics cancellation. (a) Capacitor voltages, (b) arm currents, and (c) output current i_{oa}.

The filter size is inevitably enlarged in order to attenuate this lowest harmonic group.

The switching frequency ripple on the circulating current i_{ca} is basically eliminated as shown in Figs. 9(b) and 11(b). The low-frequency second-order harmonic in the circulating current can be suppressed by adding an active circulating current controller [25]. Although there is a small voltage ripple on the SM capacitor as shown in Fig. 10(a) (<10%), the harmonic spectra still agree well with the theoretical analysis. Therefore, the assumption made in Section III is reasonable, in which the capacitor voltages are assumed to be well balanced.

Figs. 12 and 14 show the simulated results of the hybrid MMC using the traditional PSC-PWM scheme for the output voltage harmonics minimization. Fig. 12 shows the phase voltage u_{oa} and the circulating current waveform i_{ca}. Fig. 13 shows the capacitors voltages, the arm currents, and the output current waveform.

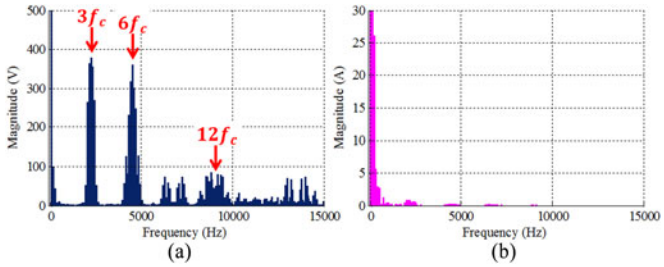

Fig. 11. Harmonics spectra of hybrid MMC using traditional PSC-PWM scheme for circulating current harmonics cancellation. (a) Phase voltage u_{oa} and (b) circulating current i_{ca}.

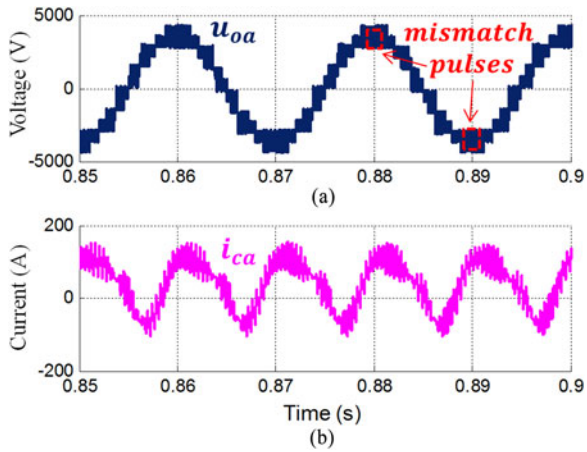

Fig. 12. Simulated waveforms of hybrid MMC using traditional PSC-PWM scheme for output voltage harmonics minimization. (a) Phase voltage u_{oa} and (b) circulating current i_{ca}.

Although there are some mismatch pulses on the phase voltage u_{oa} as shown in Fig. 12(a) due to the different output equivalent switching frequencies of the HBSMs and the FBSMs, the switching frequency harmonic is basically eliminated as shown in Fig. 14(a). The center frequency of the lowest harmonic group of the phase voltage is 4500 Hz ($6f_{\mathrm{c}} = 6 \times 750$ Hz) as shown in Fig. 14(a), which agrees well with the theoretical analysis given by (24). The switching harmonics are shown on the circulating current waveform as shown in Fig. 12(a).The center frequency of the lowest harmonic group of the circulating current is 2250 Hz ($3f_{\mathrm{c}} = 3 \times 750$ Hz) as shown in Fig. 14(b), which is equal to Hf_{c} as presented in Section III-A. The filter size is inevitably enlarged in order to attenuate this lowest harmonic group. The voltages of the SM capacitors are balanced as shown in Fig. 13(a).

B. Hybrid MMC With Improved PSC-PWM Scheme

The simulated results of the hybrid MMC with the improved PSC-PWM scheme are shown in Figs. 15–Fig. 20. Figs. 15 and 16 show the simulated waveforms of the hybrid MMC using the improved PSC-PWM scheme for circulating current harmonics cancellation. Fig. 15 shows the phase voltage u_{oa} and the circulating current waveform i_{ca}. Fig. 16 shows the

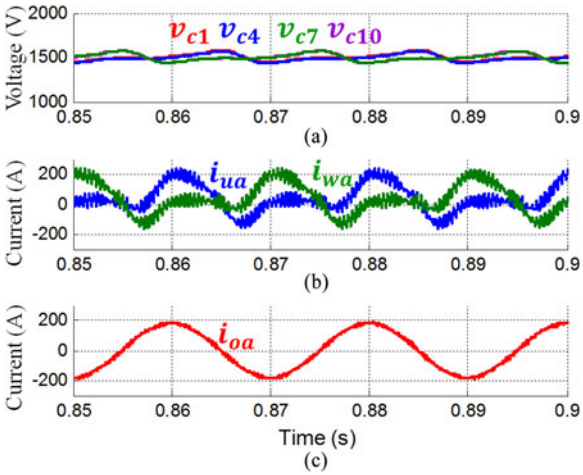

Fig. 13. Simulated waveforms of hybrid MMC using traditional PSC-PWM scheme for output voltage harmonics minimization. (a) Capacitor voltages, (b) arm currents, and (c) output current $i_{\rm oa}$.

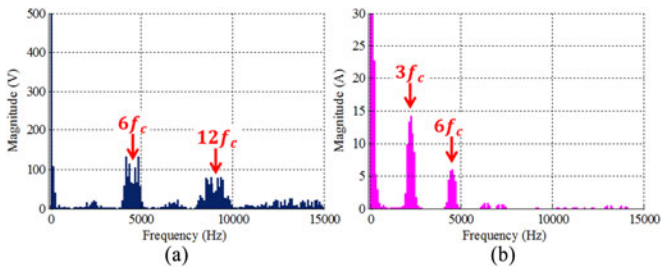

Fig. 14. Harmonics spectra of hybrid MMC using traditional PSC-PWM scheme for output voltage harmonics minimization. (a) Phase voltage $u_{\rm oa}$ and (b) circulating current $i_{\rm ca}$.

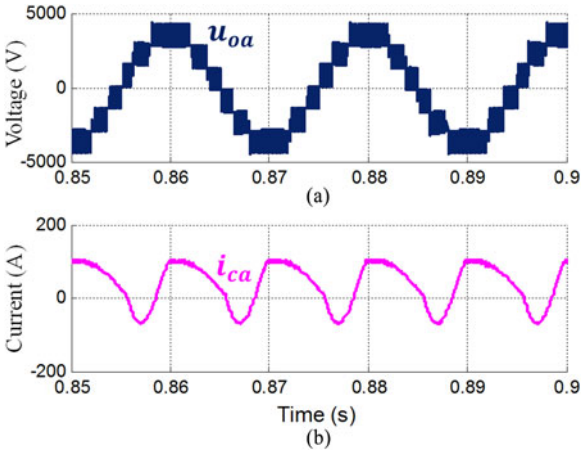

Fig. 15. Simulated waveforms of hybrid MMC using improved PSC-PWM scheme for circulating current harmonics cancellation. (a) Phase voltage $u_{\rm oa}$ and (b) circulating current $i_{\rm ca}$.

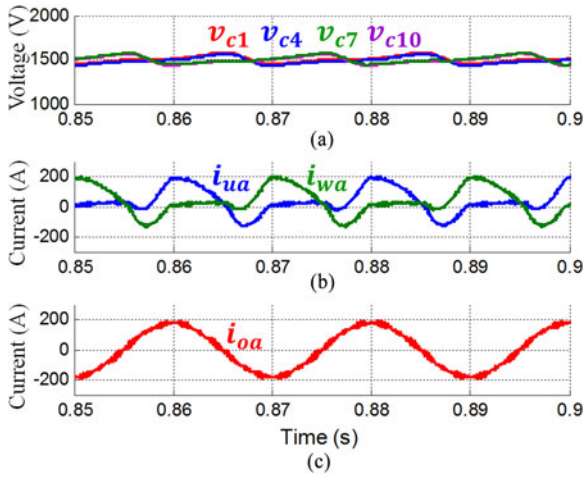

Fig. 16. Simulated waveforms of hybrid MMC using improved PSC-PWM scheme for circulating current harmonics cancellation. (a) Capacitor voltages, (b) arm currents, and (c) output current $i_{\rm oa}$.

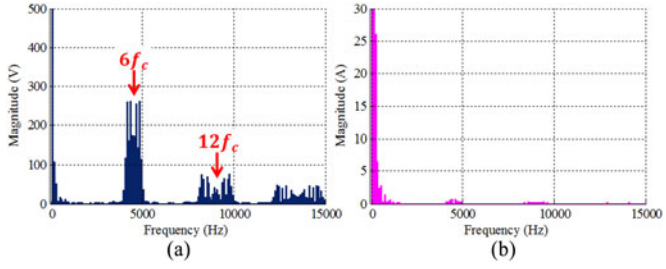

Fig. 17. Harmonics spectra of hybrid MMC using improved PSC-PWM scheme for circulating current harmonics cancellation. (a) Phase voltage $u_{\rm oa}$ and (b) circulating current $i_{\rm ca}$.

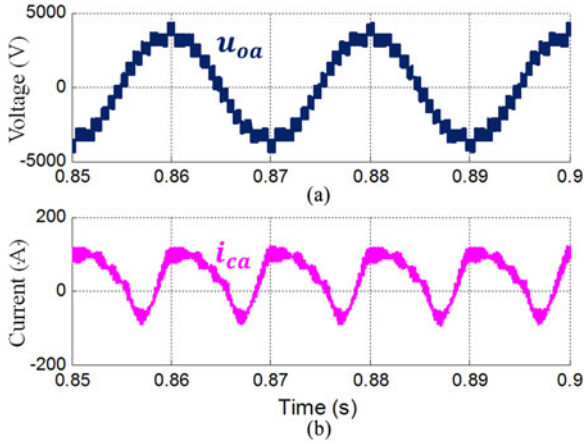

Fig. 18. Simulated waveforms of hybrid MMC using improved PSC-PWM scheme for output voltage harmonics minimization. (a) Phase voltage $u_{\rm oa}$ and (b) circulating current $i_{\rm ca}$.

capacitors voltages, the arm currents, and the output current waveform.

It can be seen that there are no mismatch pulses on the phase voltage $u_{\rm oa}$ as shown in Fig. 15(a). The center frequency of the lowest harmonic group of the phase voltage is 4500 Hz ($6f_{\rm c} = 6 \times 750$ Hz) as shown in Fig. 17(a), which equals $Nf_{\rm ch}$ as presented in Section III-B. The filter size reduction can be significantly reduced because the cutoff frequency of the filter is doubled. The switching frequency ripple on the circulating current $i_{\rm ca}$ is basically eliminated as shown in Figs. 15(b) and 17(b). The SM capacitor voltages are also balanced as shown in Fig. 16(a).

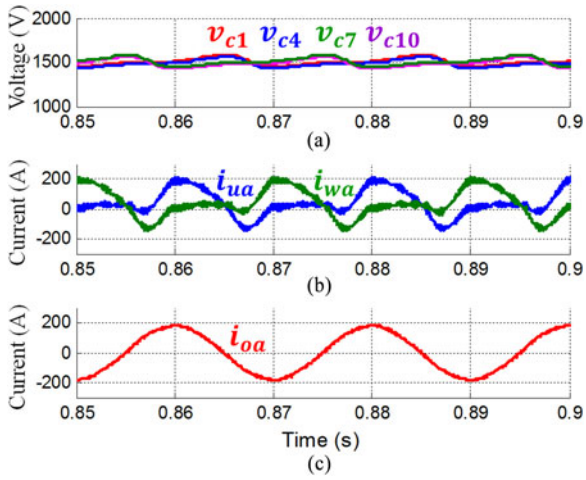

Fig. 19. Simulated waveforms of hybrid MMC using improved PSC-PWM scheme for output voltage harmonics minimization. (a) Capacitor voltages, (b) arm currents, and (c) output current i_{oa}.

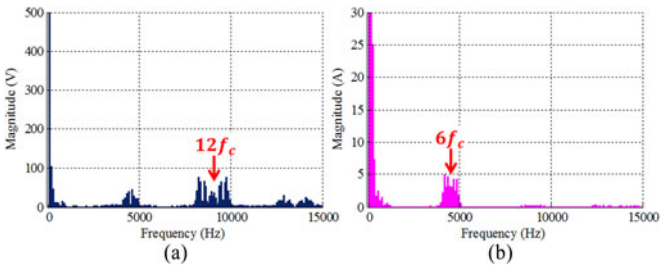

Fig. 20. Harmonics spectra of hybrid MMC using improved PSC-PWM scheme for output voltage harmonics minimization. (a) Phase voltage u_{oa} and (b) circulating current i_{ca}.

Figs. 18 and 20 show the experimental waveforms of the hybrid MMC using the improved PSC-PWM scheme for the output voltage harmonics minimization. The output voltage is a 13-level waveform and there are no mismatch pulses on the phase voltage u_{oa} as shown in Fig. 18(a), the switching frequency harmonic is basically eliminated as shown in Fig. 20(a). The center frequency of the lowest harmonic group of the output voltage is 9 kHz ($12f_{\mathrm{c}} = 12 \times 750$ Hz), which agrees well with theoretical analysis given in (49). The frequency of the switching harmonics on the circulating current waveform is higher than the traditional PSC-PWM, which is shown in Fig. 18(a). The center frequency of the lowest harmonic group of the circulating current is 4.5 kHz ($6f_{\mathrm{c}} = 6 \times 750$ Hz) as shown in Fig. 20(b), which equals Nf_{ch} as illustrated in Section III-B.

Based on the simulated results, it can be seen the improved PSC-PWM scheme for the hybrid MMC can make the center frequency of the lowest harmonics group become higher compared with the traditional PSC-PWM scheme for the hybrid MMC. The cutoff frequency of the filter can be increased accordingly. Therefore, the size of the filter can be reduced.

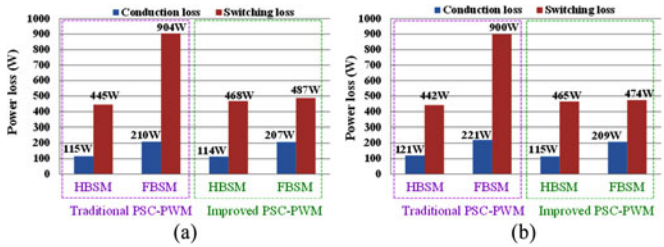

Fig. 21. Loss distributions for different PSC-PWM schemes. (a) PSC-PWM schemes with circulating current harmonics cancellation and (b) PSC-PWM schemes with output voltage harmonics minimization.

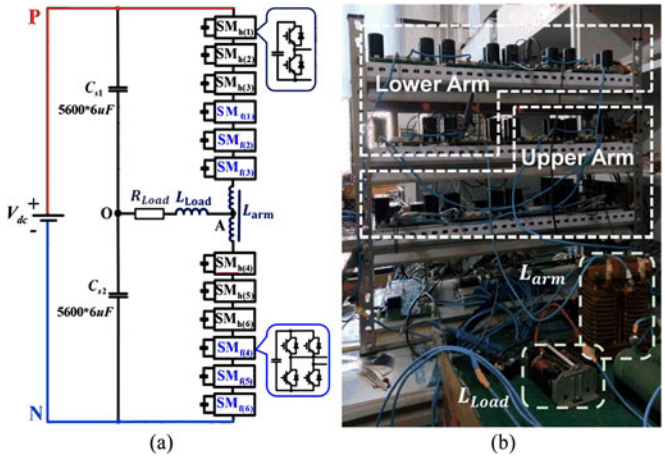

Fig. 22. Schematic and picture of hybrid MMC prototype. (a) Prototype schematic and (b) prototype picture.

C. Loss Reduction and Loss Distribution Comparison

To investigate the loss distribution of the HBSMs and the FBSMs, a simple loss calculation method is employed [34]. The loss calculation is embedded into the simulation model of the hybrid MMC with the main parameters given in Table I. The parameters of the semiconductor module, FZ800R33KL2C, are used in the calculation. The loss distributions of the HBSM and the FBSM in the same arm under the different PSC-PWM schemes are shown in Fig. 21.

It can be seen that the loss distribution between the HBSMs and the HBSMs is very uneven in the traditional PSC-PWM schemes because the total switching loss of the FBSM is double that of the HBSM. The switching frequency of the FBSMs in the improved PSC-PWM scheme is reduced to half that of the traditional PSC-PWM scheme. Therefore, the total switching loss of the FBSMs in the improved PSC-PWM schemes is reduced by half. Accordingly, the loss distribution between the HBSMs and the FBSMs is much even in the improved PSC-PWM scheme.

V. Experimental Results Verification

In order to verify the theoretical analysis and simulation results, a hybrid MMC prototype is built as shown in Fig. 22. The parameters of the prototype are tabulated in Table II. Each arm contains three HBSMs and three FBSMs. A coupled inductor

TABLE II
PARAMETERS OF HYBRID MMC PROTOTYPE

Parameters	Values	Parameters	Values
Rated active power P	622 W	Unit capacitance constant [44] H	79 ms
DC-link voltage $V_{\rm dc}$	300 V	Carrier frequency $f_{\rm c}$	750 Hz
Number of SMs per arm N	6	Carrier frequency for HBSMs $f_{\rm ch}$	750 Hz
Number of HBSMs per arm H	3	Carrier frequency for FBSMs $f_{\rm cf}$	375 Hz
Number of FBSMs per arm F	3	Fundamental frequency f_0	50 Hz
Rated SM Capacitor voltage $U_{\rm c}$	50 V	Load resistance $R_{\rm Load}$	12 Ω
Arm inductance $L_{\rm u} = L_{\rm w} = M = L_{\rm o}$	0.625 mH (1.6%)	Load inductance $L_{\rm Load}$	1 mH (2.6%)
SM Capacitance C	3280 μF	Output ac current	7.2 A (rms)

Values in () are on a single-phase 86-V, 7.2-A, and 50-Hz base.

is employed as the arm inductor and a resistive load is used in the experiment. The carrier frequency for the HBSMs and the FBSMs under the traditional PSC-PWM scheme is 750 Hz. The carrier frequencies for the HBSMs and FBSMs under the improved PSC-PWM scheme are 750 and 375 Hz, respectively.

The digital-signal-processor (DSP) TMS320F28335 is used as the controller, which executes the control algorithms for the MMC [44] and generates PWM signals for the SMs. The PWM synchronization in the traditional PSC-PWM is achieved by every $T_c(T_c = 1/f_c)$, while the PWM synchronization in the improved PSC-PWM is achieved by every $T_{\rm cf}(T_{\rm cf} = 1/f_{\rm cf})$. The duty cycles of the SMs are updated by every $T_c/2(T_c = 1/f_c = 1/f_{\rm ch})$ for both the traditional PSC-PWM and the improved PSC-PWM. An EP4CE15F17C8N FPGA is used as the interface between the DSP and the SMs. The PWM signals generated by DSP are distributed to the SMs by FPGA via optical fibers, while the capacitor voltages of the SMs are collected and transferred to DSP via the FPGA.

A. Hybrid MMC With Circulating Current Harmonics Cancellation

The experimental results of the hybrid MMC with the circulating current harmonics cancellation are shown in Figs. 23 and 24. Fig. 23(a) and (b) shows the experimental waveforms of the hybrid MMC using the traditional PSC-PWM scheme for the circulating current harmonics cancellation. Fig. 23(c) and (d) shows the experimental waveforms of the hybrid MMC using the improved PSC-PWM scheme for the circulating current harmonics cancellation.

Both two PSC-PWM schemes have the circulating current harmonics cancellation effect. The mismatch pulses on the phase voltage $u_{\rm oa}$ are eliminated by using the improved PSC-PWM as shown in Fig. 23(c). The capacitor voltages of these two cases are well balanced as shown in Fig. 23(b) and (d). The output current ripple of the improved PSC-PWM scheme is also smaller than that of the traditional PSC-PWM scheme. The FFT analysis of the phase voltages and the circulating currents are shown in Fig. 24. Fig. 24(a) and (b) shows the FFT analysis of the phase voltage and the circulating current for the hybrid MMC

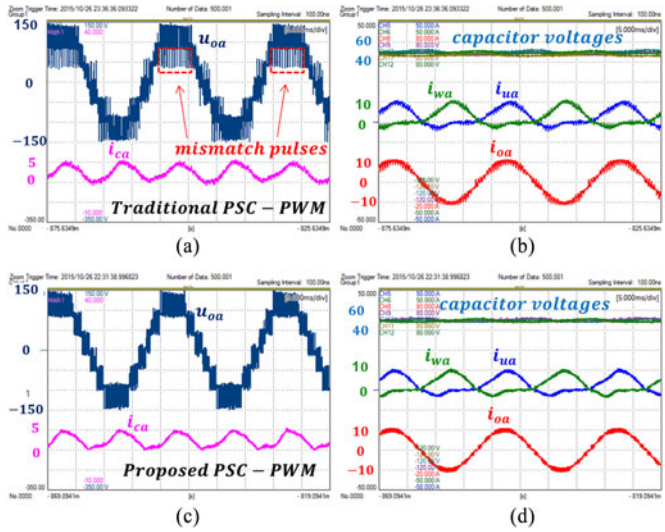

Fig. 23. Experimental waveforms of hybrid MMC with circulating current harmonics cancellation. (a) Phase voltage $u_{\rm oa}$ and circulating current $i_{\rm ca}$ of traditional PSC-PWM, (b) SM capacitor voltages, lower arm current i_{wa}, upper arm current i_{ua}, and phase current $i_{\rm oa}$ of traditional PSC-PWM, (c) phase voltage $u_{\rm oa}$ and circulating current $i_{\rm ca}$ of improved PSC-PWM, and (d) SM capacitor voltages, lower arm current i_{wa}, upper arm current i_{ua}, and phase current $i_{\rm oa}$ of improved PSC-PWM.

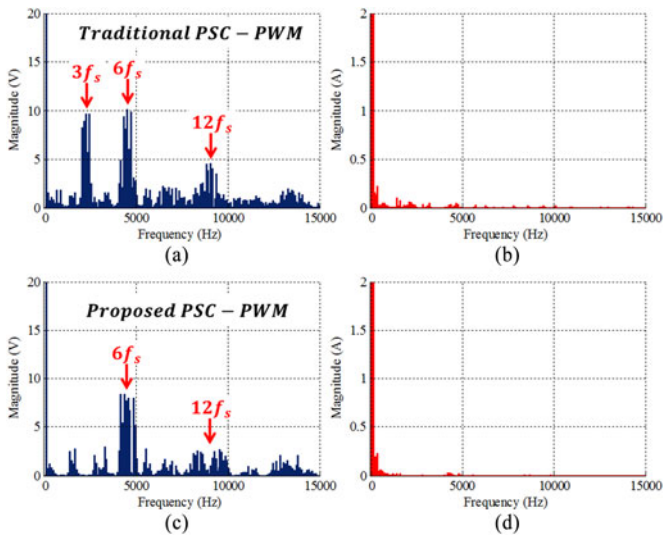

Fig. 24. Harmonics spectra of hybrid MMC using with circulating current harmonics cancellation. (a) Phase voltage $u_{\rm oa}$ of traditional PSC-PWM, (b) circulating current $i_{\rm ca}$ of traditional PSC-PWM, (c) phase voltage $u_{\rm oa}$ of improved PSC-PWM, and (d) circulating current $i_{\rm ca}$ of the improved PSC-PWM.

using the traditional PSC-PWM scheme with the circulating current harmonics cancellation. Fig. 24(c) and (d) shows the FFT analysis of the phase voltage and the circulating current for the improved PSC-PWM scheme with the circulating current harmonics cancellation.

For the traditional PSC-PWM scheme, the center frequency of the lowest harmonic group of the phase voltage is 2250 Hz ($3f_{\rm c} = 3 \times 750$ Hz) as shown in Fig. 24(a). For the improved PSC-PWM scheme, the center frequency of the lowest harmonic group of the phase voltage is 4500 Hz ($6f_{\rm c} = 6 \times 750$ Hz) as

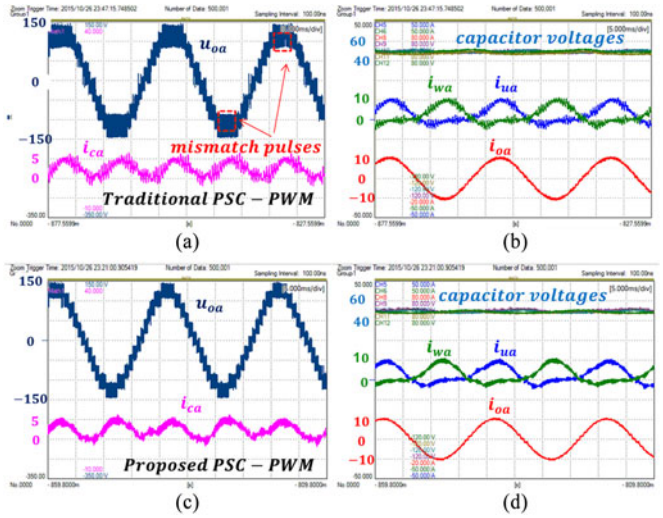

Fig. 25. Experimental waveforms of hybrid MMC with output voltage harmonics minimization. (a) Phase voltage $u_{\rm oa}$ and circulating current $i_{\rm ca}$ of traditional PSC-PWM, (b) SM capacitor voltages, lower arm current i_{wa}, upper arm current i_{ua}, and phase current $i_{\rm oa}$ of traditional PSC-PWM, (c) phase voltage $u_{\rm oa}$ and circulating current $i_{\rm ca}$ of improved PSC-PWM, and (d) SM capacitor voltages, lower arm current i_{wa}, upper arm current i_{ua}, and phase current $i_{\rm oa}$ of improved PSC-PWM.

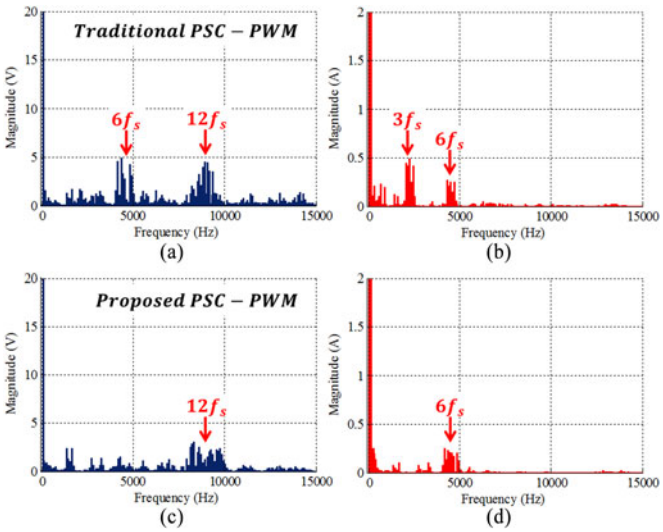

Fig. 26. Harmonics spectra of hybrid MMC using with output voltage harmonics minimization. (a) Phase voltage $u_{\rm oa}$ of traditional PSC-PWM, (b) circulating current $i_{\rm ca}$ of traditional PSC-PWM, (c) phase voltage $u_{\rm oa}$ of improved PSC-PWM, and (d) circulating current $i_{\rm ca}$ of improved PSC-PWM.

shown in Fig. 24(c). The experimental results match with the theoretical analysis and the simulation results. The switching frequency ripples on the circulating current $i_{\rm ca}$ are basically eliminated in both two cases as shown in Fig. 24(b) and (d).

B. Hybrid MMC With Output Voltage Harmonics Minimization

Figs. 25 and 26 show the experimental waveforms of the hybrid MMC with output voltage harmonics minimization. Fig. 25(a) and (b) shows the experimental waveforms of the hybrid MMC using the traditional PSC-PWM scheme for the output voltage harmonics minimization. Fig. 25(c) and (d) shows the experimental waveforms of the hybrid MMC using the improved PSC-PWM scheme for the output voltage harmonics minimization.

Both two PSC-PWM schemes have 13-level output phase voltage, and a good output current waveform. The mismatch pulses on the phase voltage $u_{\rm oa}$ are eliminated by using the improved PSC-PWM as shown in Fig. 25(c). The capacitor voltages of these two cases are well balanced. The circulating current ripple of the improved PSC-PWM scheme is smaller than that of the traditional PSC-PWM scheme. The FFT analysis of the phase voltages and the circulating currents are shown in Fig. 26. Fig. 26(a) and (b) shows the FFT analysis of the phase voltage and the circulating current for the hybrid MMC using the traditional PSC-PWM scheme with the circulating current harmonics cancellation. Fig. 26(c) and (d) shows the FFT analysis of the phase voltage and the circulating current for the improved PSC-PWM scheme with the circulating current harmonics cancellation.

For the traditional PSC-PWM scheme, the center frequency of the lowest harmonic group of the phase voltage is 4500 Hz ($6f_{\rm c} = 6 \times 750$ Hz) as shown in Fig. 26(a). For the improved PSC-PWM scheme, the center frequency of the lowest harmonic group of the phase voltage is 9000 Hz ($12f_{\rm c} = 12 \times 750$ Hz) as shown in Fig. 26(c). The switching harmonics are shown on the circulating current as shown in Fig. 26(b) and (d). However, the center frequency of the lowest harmonic group of the circulating current is 2250 Hz ($3f_{\rm c} = 3 \times 750$ Hz) for the traditional PSC-PWM scheme, while it is 4500 Hz ($6f_{\rm c} = 6 \times 750$ Hz) for the improved PSC-PWM scheme. The experimental results match with the theoretical analysis and the simulation results.

C. Comparison Between Simulation and Experimental Results

The simulation is based on a 1-MW scenario, while the experimental set up is the scaledown prototype of the simulation. The unit capacitance constant of the experimental set up is close to that in the simulation. The same value of inductances of the arm inductor and the output inductor with respect to the base value are selected. Both the simulation and the experiment verify the theoretical analysis and show the advantages of the improved PSC-PWM compared with the traditional PSC-PWM. Due to some nonideal factors (dead time, sensor noises, sampling delay, etc) in the real experiment, the harmonic spectra of the experimental results is not so "clean" compared with the simulation results. However, the advantages of the improved PSC-PWM compared with the traditional PSC-PWM are still illustrated.

VI. Conclusion

In this paper, an improved PSC-PWM scheme is proposed for the hybrid MMC which consists of the HBSMs and the FBSMs. The traditional PSC-PWM schemes used in the HBSMs-based MMC and the FBSMs-based MMC are directly applied to the hybrid MMC and the harmonic characters are analyzed by using the double Fourier analysis. It is found that some mismatch pulses will occur on the arm voltages, which not only generates

undesirable harmonics on the output voltages, but also induces the significantly uneven loss distributions between the HBSMs and the FBSMs. Therefore, an improved PSC-PWM scheme is proposed to deal with these issues by reducing the switching frequency of the FBSM to half that of the HBSM and applying a proper phase-shifting angle between the HBSMs and the FBSMs. The improved PSC-PWM scheme can eliminate the mismatch pulses in the output voltages, alleviate the uneven loss distributions between the HBSMs and the FBSMs, and reduce the total switching loss of the converter. The harmonic characters of the improved PSC-PWM are investigated by using the double Fourier analysis. The optimum displacement angles between the upper arm and the lower arm for either the output voltage harmonics minimization or the circulating current harmonics cancellation are also specified. The analysis results are verified by both the simulation results and the experimental results.

REFERENCES

[1] R. Marquardt, "Stromrichterschaltungen mit verteilten energiespeichern," German Patent DE10103031A1, Jan. 24, 2001.

[2] A. Nami, J. Liang, F. Dijkhuizen, and G. D. Demetriades, "Modular multilevel converters for HVDC applications: Review on converter cells and functionalities," *IEEE Trans. Power Electron.*, vol. 30, no. 1, pp. 18–36, Jan. 2015.

[3] M. A. Perez, S. Bernet, J. Rodriguez, S. Kouro, and R. Lizana, "Circuit topologies, modeling, control schemes, and applications of modular multilevel converters," *IEEE Trans. Power Electron.*, vol. 30, no. 1, pp. 4–17, Jan. 2015.

[4] C. Oates, "Modular multilevel converter design for VSC HVDC applications," *IEEE J. Emerg. Sel. Topics Power Electron.*, vol. 3, no. 2, pp. 505–515, Jun. 2015.

[5] A. Lesnicar and R. Marquardt, "A new modular voltage source inverter topology," in *Proc. 10th Power Electron. Appl. Conf.*, 2003, pp. 1–10.

[6] A. Lesnicar and R. Marquardt, "An innovative modular multilevel converter topology suitable for a wide power range," presented at the IEEE Power Tech Conf., Bologna, Italy, Jun. 23–26, 2003, vol. 3.

[7] X. Li, Q. Song, W. Liu, H. Rao, S. Xu, and L. Li, "Protection of nonpermanent faults on DC overhead lines in MMC-based HVDC systems," *IEEE Trans. Power Del.*, vol. 28, no. 1, pp. 483–490, Jan. 2013.

[8] G. P. Adam and B. W. Williams, "Half- and full-bridge modular multilevel converter models for simulations of full-scale HVDC links and multiterminal DC grids," *IEEE J. Emerg. Sel. Topics Power Electron.*, vol. 2, no. 4, pp. 1089–1108, Dec. 2014.

[9] G. Adam and I. Davidson, "Robust and generic control of full-bridge modular multilevel converter high-voltage DC transmission systems," *IEEE Trans. Power Del.*, vol. 30, no. 6, pp. 2468–2476, Dec. 2015.

[10] R. Marquardt, "Modular multilevel converter: An universal concept for HVDC-networks and extended DC-bus-applications," in *Proc. IEEE Int. Power Electron. Conf.*, Jun. 21–24, 2010, pp. 502–507.

[11] X. Li, W. Liu, Q. Song, H. Rao, and S. Xu, "An enhanced MMC topology with DC fault ride-through capability," in *Proc. 39th IEEE Annu. Conf. Ind. Electron. Soc.*, Nov. 10–13, 2013, pp. 6182–6188.

[12] J. Qin, M. Saeedifard, A. Rockhill, and R. Zhou, "Hybrid design of modular multilevel converters for HVDC systems based on various submodule circuits," *IEEE Trans. Power Del.*, vol. 30, no. 1, pp. 385–394, Feb. 2015.

[13] A. Nami, L. Wang, F. Dijkhuizen, and A. Shukla, "Five level cross connected cell for cascaded converters," in *Proc. 15th Eur. Conf. Power Electron. Appl.*, Sep. 2–6, 2013, pp. 1–9.

[14] R. Marquardt, "Modular multilevel converter topologies with DC-short circuit current limitation," in *Proc. IEEE Int. Conf. Power Electron. ECCE Asia*, May 30/Jun. 3, 2011, pp. 1425–1431.

[15] S. Cui, S. Kim, J. Jung, and S. Sul, "Principle, control and comparison of modular multilevel converters (MMCs) with DC short circuit fault ride-through capability," in *Proc. IEEE 29th Annu. Appl. Power Electron. Conf.*, Mar. 16–20, 2014, pp. 610–616.

[16] S. Inoue and S. Katosh, "Modular multilevel converter with DC fault protection," European Patent EP2602927A2, Dec. 6, 2013.

[17] G. P. Adam, K. H. Ahmed, and B. W. Williams, "Mixed cells modular multilevel converter," in *Proc. IEEE Int. Symp. Ind. Electron.*, Jun. 1–4, 2014, pp. 1390–1395.

[18] M. Hagiwara, R. Maeda, and H. Akagi, "Theoretical analysis and control of the modular multilevel cascade converter based on double-star chopper-cells (MMCC-DSCC),"in *Proc. IEEE Int. Power Electron. Conf.*, Jun. 21–24, 2010, pp. 2029–2036.

[19] A. J. Korn, M. Winkelnkemper, P. Steimer, and J. W. Kolar, "Capacitor voltage balancing in modular multilevel converters," in *Proc. 6th IET Int. Conf. Power Electron. Mach. Drives*, Mar. 27–29, 2012, pp. 1–5.

[20] L. Zhang and G. Wang, "Voltage balancing control of a novel modular multilevel converter," in *Proc. IEEE 4th Int. Conf. Electr. Utility Deregulation Restruct. Power Technol.*, Jul. 6–9, 2011, pp. 109–114.

[21] R. Darus, J. Pou, G. Konstantinou, S. Ceballos, R. Picas, and V. G. Agelidis, "A modified voltage balancing algorithm for the modular multilevel converter: Evaluation for staircase and phase-disposition PWM," *IEEE Trans. Power Electron.*, vol. 30, no. 8, pp. 4119–4127, Aug. 2015.

[22] P. M. Meshram and V. B. Borghate, "A simplified nearest level control (NLC) voltage balancing method for modular multilevel converter (MMC)," *IEEE Trans. Power Electron.*, vol. 30, no. 1, pp. 450–462, Jan. 2015.

[23] Q. Tu, Z. Xu, and J. Zhang, "Circulating current suppressing controller in modular multilevel converter," in *Proc. IEEE 36th Ind. Electron. Soc. Conf.*, Nov. 7–10, 2010, pp. 3198–3202.

[24] Z. Li, P. Wang, Z. Chu, H. Zhu, Y. Luo, and Y. Li, "An inner current suppressing method for modular multilevel converters," *IEEE Trans. Power Electron.*, vol. 28, no. 11, pp. 4873–4879, Nov. 2013.

[25] M. Zhang, L. Huang, W. Yao, and Z. Lu, "Circulating harmonic current elimination of a CPS-PWM-based modular multilevel converter with a plug-in repetitive controller," *IEEE Trans. Power Electron.*, vol. 29, no. 4, pp. 2083–2097, Apr. 2014.

[26] L. He, K. Zhang, J. Xiong, and S. Fan, "A repetitive control scheme for harmonic suppression of circulating current in modular multilevel converters," *IEEE Trans. Power Electron.*, vol. 30, no. 1, pp. 471–481, Jan. 2015.

[27] N. Thitichaiworakorn, M. Hagiwara, and H. Akagi, "Experimental verification of a modular multilevel cascade inverter based on double-star bridge-cells (MMCI-DSBC)," in *Proc. IEEE Energy Convers. Congr. Expo.*, Sep. 15–20, 2012, pp. 4196 –4202.

[28] R. Zeng, L. Xu, L. Yao, and B. W. Williams, "Design and operation of a hybrid modular multilevel converter," *IEEE Trans. Power Electron.*, vol. 30, no. 3, pp. 1137–1146, Mar. 2015.

[29] R. Zeng, L. Xu, L. Yao, and J. Morrow, "Pre-charging and DC fault ride-through of hybrid MMC Based MMC-HVDC systems," *IEEE Trans. Power Del.*, vol. 30, no. 3, pp. 1298–1306, Jun. 2015.

[30] S. Debnath, J. Qin, B. Bahrani, M. Saeedifard, and P. Barbosa, "Operation, control, and applications of the modular multilevel converter: A review," *IEEE Trans. Power Electron.*, vol. 30, no. 1, pp. 37–53, Jan. 2015.

[31] K. Ilves, A. Antonopoulos, S. Norrga, and H. Nee, "A new modulation method for the modular multilevel converter allowing fundamental switching frequency," in *Proc. IEEE Int. Conf. Power Electron. ECCE Asia*, May 30/Jun. 3, 2011, pp. 991–998.

[32] Q. Tu and Z. Xu, "Impact of sampling frequency on harmonic distortion for modular multilevel converter," *IEEE Trans. Power Del.*, vol. 26, no. 1, pp. 298–306, Jan. 2011.

[33] P. Hu and D. Jiang, "A level-increased nearest level modulation method for modular multilevel converters," *IEEE Trans. Power Electron.*, vol. 30, no. 4, pp. 1836–1842, Apr. 2015.

[34] S. Rohner, S. Bernet, M. Hiller, and R. Sommer, "Modulation, losses, and semiconductor requirements of modular multilevel converters," *IEEE Trans. Ind. Electron.*, vol. 57, no. 8, pp. 2633–2642, Aug. 2010.

[35] H. Saad, J. Peralta, S. Dennetiere, J. Mahseredjian, J. Jatskevich, J. A. Martinez, A. Davoudi, M. Saeedifard, V. Sood, X. Wang, J. Cano, and A. Mehrizi-Sani, "Dynamic averaged and simplified models for MMC-based HVDC transmission systems," *IEEE Trans. Power Del.*, vol. 28, no. 3, pp. 1723–1730, Jul. 2013.

[36] G. P. Adam, O. Anaya-Lara, G. M. Burt, D. Telford, B. W. Williams, and J. R. McDonald, "Modular multilevel inverter: Pulse width modulation and capacitor balancing technique," *IET Power Electron.*, vol. 3, pp. 702–715, Sep. 2010.

[37] S. Kouro, M. Malinowski, K. Gopakumar, J. Pou, L. G. Franquelo, W. Bin, J. Rodriguez, M. A. Perez, and J. I. Leon, "Recent advances and industrial applications of multilevel converters," *IEEE Trans. Ind. Electron.*, vol. 57, no. 8, pp. 2553–2580, Aug. 2010.

[38] M. Hagiwara and H. Akagi, "Experiment and simulation of a modular push–pull PWM converter for a battery energy storage system," *IEEE Trans. Ind. Appl.*, vol. 50, no. 2, pp. 1131–1140, Mar./Apr. 2014.
[39] R. Darus, G. Konstantinou, J. Pou, S. Ceballos, and V. G. Agelidis, "Comparison of phase-shifted and level-shifted PWM in the modular multilevel converter," in *Proc. IEEE Int. Power Electron. Conf. ECCE Asia*, May 18–21, 2014, pp. 3764–3770.
[40] B. Li, R. Yang, D. Xu, G. Wang, W. Wang, and D. Xu, "Analysis of the phase-shifted carrier modulation for modular multilevel converters," *IEEE Trans. Power Electron.*, vol. 30, no. 1, pp. 297–310, Jan. 2015.
[41] K. Ilves, L. Harnefors, S. Norrga, and H. P. Nee, "Analysis and operation of modular multilevel converters with phase-shifted carrier PWM," *IEEE Trans. Power Electron.*, vol. 30, no. 1, pp. 268–283, Jan. 2015.
[42] M. Hagiwara, R. Maeda, and H. Akagi, "Control and analysis of the modular multilevel cascade converter based on double-star chopper-cells (MMCC-DSCC)," *IEEE Trans. Power Electron.*, vol. 26, no. 6, pp. 1649–1658, Jun. 2011.
[43] D. G. Holmes and B. P. McGrath, "Opportunities for harmonic cancellation with carrier-based PWM for a two-level and multilevel cascaded inverters," *IEEE Trans. Ind. Appl.*, vol. 37, no. 2, pp. 574–582, Mar./Apr. 2001.
[44] M. Hagiwara and H. Akagi, "Control and experiment of pulsewidth-modulated modular multilevel converters," *IEEE Trans. Power Electron.*, vol. 24, no. 7, pp. 1737–1746, Jul. 2009.

Sizhao Lu (S'13) received the B.S. and M.S. degrees in electrical engineering from the Harbin Institute of Technology, Harbin, China, in 2008 and 2010, respectively. He is currently working toward the Ph. D. degree at the Department of Electrical Engineering, Tsinghua University, Beijing, China.

From February 2012 to November 2013, he was a Visiting Scholar with the Center for Power Electronics Systems, Virginia Tech, Blacksburg, VA, USA. His research interests include modular multilevel converters and high-frequency high-power three-level dc–dc converters.

Liqiang Yuan (M'09) received the B.S. and Ph.D. degrees from Tsinghua University, Beijing, China, in 1999 and 2004, respectively.

He became an Assistant Professor in 2004 and an Associate Professor in 2008 with the Department of Electrical Engineering, Tsinghua University, where he is currently the Deputy Director at the Institute of Power Electronics and Motor System. His research interests include application techniques of semiconductor devices, solid-state transformer, and high-power high-voltage converters.

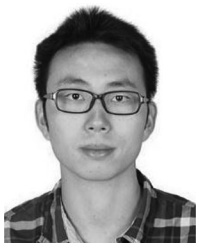

Kai Li (S'13) received the B.S. degree in electrical engineering from Wuhan University, Hubei, China, in 2011. Since 2011, he has been working toward the Ph.D. degree at the Department of Electrical Engineering, Tsinghua University, Beijing, China.

From September 2013 to February 2015, he was a Visiting Scholar with the Center for Power Electronics Systems, Virginia Tech, Blacksburg, VA, USA. His research interests include modular multilevel converters, PWM strategies, and reliability of power electronics converters.

Zhengming Zhao (M'02–SM'03) received the B.S. and M.S. degrees in electrical engineering from Hunan University, Changsha, China, in 1982 and 1985, respectively, and the Ph.D. degree from Tsinghua University, Beijing, China, in 1991.

In 1991, he joined the Department of Electrical Engineering, Tsinghua University. From 1994 to 1996, he was a Postdoctoral Fellow with The Ohio State University, Columbus, OH, USA, and then was a Visiting Scholar with the University of California, Irvine, CA, USA, for one year. He is currently a Professor at the Department of Electrical Engineering and the Deputy Director at the State Key Laboratory of Power System, Tsinghua University. His research interests include high-power conversion, power electronics and motor control, and solar energy applications.

Prof. Zhao is a Fellow of the Institution of Engineering and Technology, U.K. He is also the Vice-President of the Beijing Power Electronics Society and the Chairman of the IEEE Power Electronics Society Beijing Chapter.